Quantifying air-sea heat fluxes over Southeast Asia and their response to climate change

Hue Nguyen-Thanh, Thanh Ngo-Duc, Marine Herrmann

Quantifying air–sea heat fluxes over Southeast Asia and their response to climate change

Article · July 2025

DOI: 10.1175/JCLI-D-24-0389.1

3 authors:

Hue Thi Thanh Nguyen
The University of Texas at Arlington
5 PUBLICATIONS **28** CITATIONS
SEE PROFILE

Thanh Ngo-Duc
University of Science and Technology of Hanoi
125 PUBLICATIONS **4,667** CITATIONS
SEE PROFILE

Marine Herrmann
Institute of Research for Development
87 PUBLICATIONS **3,509** CITATIONS
SEE PROFILE

Quantifying air-sea heat fluxes over Southeast Asia and their response to climate change

Hue Nguyen-Thanh,[a,b,c], Thanh Ngo-Duc,[a,*], Marine Herrmann,[a,b]

[a] *LOTUS Laboratory, University of Science and Technology of Hanoi (USTH), Vietnam Academy of Science and Technology (VAST), Hanoi, Vietnam*

[b] *Université de Toulouse, LEGOS (CNES/CNRS/IRD/UT3), Toulouse, France*

[c] *Department of Civil Engineering, University of Texas at Arlington, TX, USA*

Corresponding author: Thanh Ngo-Duc, ngo-duc.thanh@usth.edu.vn

File generated with AMS Word template 2.0

Early Online Release: This preliminary version has been accepted for publication in *Journal of Climate*, may be fully cited, and has been assigned DOI 10.1175/JCLI-D-24-0389.1. The final typeset copyedited article will replace the EOR at the above DOI when it is published.

ABSTRACT

This study presents an analysis of air-sea heat fluxes in Southeast Asia using outputs from 30 Coupled Model Intercomparison Project Phase 6 (CMIP6) models, evaluated against ERA5 reanalysis data. The CMIP6 multi-model ensemble mean (MME) estimation reveals that the net shortwave radiation gain for the ocean over the baseline period 1995–2014 (SW, 209 ± 6.6 Wm^{-2}) is counterbalanced by losses of latent heat flux (LH, -137.8 ± 7.2 Wm^{-2}), net longwave radiation (LW, -50.8 ± 1.7 Wm^{-2}), and sensible heat flux (SH, -13.6 ± 1.1 Wm^{-2}). The resulting annual net heat gain (Qnet) for CMIP6 MME (6.8 ± 11.4 Wm^{-2}) underestimates ERA5's result (21.3 ± 11.8 Wm^{-2}), despite a high spatial correlation (0.87) between the two products. The primary contributors to zonal and seasonal Qnet biases are discrepancies in SW and LH, followed by biases in SH and LW. Regarding the future change of heat flux under three Shared Socio-Economic Pathways (SSP) 1-2.6, 2-4.5, and 5-8.5, Qnet gain, SW gain, and LH loss are projected to significantly increase, while LW loss and SH loss are projected to weaken. Models with higher projected sea surface temperature (SST) warming tend to exhibit larger changes in heat fluxes, resulting in the highest and lowest changes obtained under SSP5-8.5 and SSP1-2.6, respectively. LW loss decreases with increasing SST due to enhanced downward longwave radiation, though this is partially offset by an increased in upward longwave radiation. The LH loss increase and SH loss decrease with increasing SST are associated with the thermodynamic effect rather than the dynamic effect over the study region.

1. Introduction

Air-sea heat fluxes (HFs) at the interface between the air and the ocean include shortwave radiation flux (SW), longwave radiation flux (LW), sensible heat flux (SH), latent heat flux (LH), and their sum referred to as the net HF (Qnet). A positive (negative value) of Qnet indicates a heat gain (loss) for the ocean, i.e. the SW gain is greater (less) than the LW, LH, and SH losses. These HFs play an important role in air-sea interactions on various scales (Yu and Weller, 2007). For instance, variations in Qnet affect the temperature and density of seawater, which can drive ocean currents and subsequently contribute to the redistribution of heat on a global scale (Cayan, 1992; Josey et al. 1999; Trenberth et al. 2009). Moreover, the heat exchanged between the ocean and the atmosphere influences key atmospheric processes, such as evaporation and convection

Accepted for publication in *Journal of Climate.* DOI 10.1175/JCLI-D-24-0389.1.

(Fairall et al. 2003; Yu 2007). As such, understanding and accurately determining Qnet across different spatio-temporal scales is crucial for correctly assessing global and regional changes. However, making accurate estimation of Qnet remains challenging due to large uncertainties in the datasets of each HF component, which are obtained from various sources such as satellite-based observations, ship-based measurements, or reanalysis data (Brunke et al., 2003; Yu et al., 2004; Zhang et al., 2004). Previous studies revealed that satellite estimates tend to exhibit a heating bias for the ocean, whereas reanalysis estimates tend to exhibit a cooling bias (Park et al., 2005; Valdivieso et al., 2017). Song and Yu (2013) indeed showed that the reanalysis group, which includes NCEP1 (Kalnay et al., 1996), NCEP2 (Kanamitsu et al., 2002), and ERA-Interim (Dee et al., 2011), exhibits relatively low Qnet values, ranging from 1 to 11 Wm^{-2} on a global average. In contrast, the ship-based product NOCSv2.0 (Berry and Kent, 2009) yields a Qnet of 25 Wm^{-2}, and the satellite-based product OAFlux + ISCCP (Yu et al., 2008; Zhang et al., 2004) indicates a Qnet of 30 Wm^{-2}.

The estimation of Qnet and its four components also relies on model outputs. Global Climate Models (GCMs) play a crucial role in providing and comparing climate projections across the different phases of the Coupled Model Intercomparison Projects (CMIP), including Phase 5 (CMIP5; Taylor et al., 2012) and Phase 6 (CMIP6; Eyring et al., 2016). These models are fundamental for understanding past, present, and future climate changes, forming the foundation of the Assessment Reports published by the Intergovernmental Panel on Climate Change (IPCC) (e.g. IPCC, 2021). Ensuring an accurate representation of HFs in these GCMs is needed for reliable climate projections and estimating HFs at the global and regional scales helps to evaluate and improve these models. CMIP5 GCMs have been shown to often overestimate LH in the tropics, although they could effectively capture LH spatial and temporal patterns (Cao et al., 2015; Zhang et al., 2018). Wild (2020) demonstrated that the multi-model means of the latest CMIP6 GCMs produced a better global average of flux components compared to previous model generations, especially regarding surface downward SW and LW radiations. Furthermore, the representation of the Wind-Evaporation-Sea surface temperature (WES) feedback in CMIP6 models, which is crucial for ensuring the reliability of future projections, has shown improvements compared to CMIP5 (Amaya et al., 2017; Xia et al., 2023).

Accepted for publication in *Journal of Climate.* DOI 10.1175/JCLI-D-24-0389.1.

It is worth mentioning that there is existing literature analyzing biases in the CMIP6 multi-model ensemble for HFs and related variables (e.g., Dhage and Widlansky, 2022; Jin et al., 2023; McKenna et al., 2024; Naskar et al. 2024), but detailed analysis and discussions specifically focusing on Southeast Asia are sorely lacking. For instance, Mckenna et al. (2024) analyzed the outputs of 20 CMIP6 GCMs and found that biases in atmospheric processes are a primary cause of biases in sea surface temperature (SST). Additionally, Naskar et al. (2024) used 12 CMIP6 GCMs over the North Indian Ocean and indicated that the future rise in LH can be attributed to an increase in SST. Previous studies have extensively investigated the role of SST in air-sea heat exchanges (Barsugli and Battisti, 1998; Gao et al., 2013; Wu et al., 2007; Zhang et al., 1995; Zhang and Mcphaden, 1995). An increase in SST results in increased evaporation, which in turn contributes to the transfer of heat from the ocean to the atmosphere by LH (Zhang and Mcphaden, 1995). It is noteworthy to mention that the relationship between LH and SST is more complex than a simple monotonic increase. As shown by Zhang and Mcphaden (1995), LH increases with SST up to a certain point, after which it levels off and tends to decrease when SST exceeds 28°C. Additionally, Kumar et al. (2017) found that for a general area in the tropics, at low SST, the change in LH and SST is primarily influenced by contributions from humidity deficit (thermodynamics), whereas at high SST, the change is dominated by contributions from wind (dynamics). However, they highlighted that the Bay of Bengal and the north Arabian Sea are exceptions to the above global relationship, attributed to strong seasonality in monsoon-related variables.

Southeast Asia (SEA), which encompasses the Maritime component, is situated in the Indo-Pacific Warm Pool region, a geographically diverse area located between the Indian Ocean and the Pacific Ocean (described in more detail in subsection 2.a). It plays a particular role in global climate dynamics. The climatic conditions prevailing across SEA land are primarily characterized by high temperatures and humidity, significantly influenced not only by the monsoonal circulation patterns (Matsumoto, 1997; Tangang et al., 2020; Juneng and Tangang, 2005), but also by factors such as the seasonal shift of the Intertropical Convergence Zone (ITCZ) (Schneider et al., 2014), large-scale drivers like the Walker circulation, the Madden-Julian Oscillation (MJO), the El Niño Southern Oscillation (ENSO), the Indian Ocean Dipole and other oceanic factors such as SST (Xavier et al., 2014; Magnaye et al., 2023; Nguyen-Thanh et al., 2023; Nguyen-Le et al. 2024). Conversely, the air-sea coupling processes involved in the functioning of SEA

Accepted for publication in *Journal of Climate.* DOI 10.1175/JCLI-D-24-0389.1.

climate significantly influence those large-scale climate phenomena. Prior studies demonstrated that SST is related to the monsoon strength and patterns (Meehl, 1994; Yang and Lau, 1998), thereby interconnected with precipitation patterns in the region through air-sea interactions (Chang et al., 2000; Ngo-Thanh et al., 2018; Nguyen-Le et al., 2015; Nguyen-Thanh et al., 2023). Hence, to better understand the behaviors and changes in the SEA climate, it is important to accurately understand and represent air-sea interactions, specifically HFs. However, determining the exact HF values over SEA remains challenging. The oceanic region in SEA is a heat gain area, showing a considerable range of Qnet estimates, particularly over the western marginal part of the Western Pacific Ocean with estimates ranging from 10 to 50 Wm^{-2} (Qu et al., 2004, 2006; Song and Yu, 2013; Valdivieso et al., 2017; Wang et al., 2019). In terms of future trends, earlier investigations in the SEA region have only focused on changes in specific variables such as rainfall (Ngai et al., 2022; Supari et al., 2020; Tangang et al., 2020) or surface wind (Herrmann et al., 2020; 2022). No study to date has thoroughly quantified HFs over SEA, particularly regarding their future trends across various greenhouse gas concentration scenarios.

In this study, we analyze and discuss the representation of HFs over SEA using the latest CMIP6 GCMs. Firstly, we examine the historical characteristics of HFs. Secondly, we investigate future changes in HFs, particularly in connection with SST changes. Lastly, we explore how the dynamic processes of HFs vary across a range of SST values in the region.

2. Data and methodology

a. STUDY AREA

Southeast Asia (SEA) is located in the Indo-Pacific Warm Pool region where high SST persists, supporting year-round moisture and convective activity (De Deckker, 2016). The extreme geographic limits of SEA's land are as follows: the northernmost point at approximately 28.54°N latitude in Myanmar, the southernmost point at approximately 11°S latitude on Dana Island (Indonesia), the westernmost point at approximately 141.05°E in Myanmar, and the easternmost point at approximately 141.05°E near the border between Indonesia and Papua New Guinea (Fig. 1). Over land, a large part of SEA consists of mountainous terrain, with various rivers that shape some

Accepted for publication in *Journal of Climate.* DOI 10.1175/JCLI-D-24-0389.1.

of the region's most substantial deltas. Desmet and Ngo-Duc (2022) divided SEA's land into three main sub-regions: Indochina, the Maritime Continent, and the Philippines. Indochina, comprising Cambodia, Laos, Myanmar, Thailand, and Vietnam, is part of the Asian summer monsoon region (Matsumoto, 1997) and is distinct from the Maritime Continent (including Peninsular Malaysia), which is more influenced by the Australian summer monsoon occurring during the boreal winter (Juneng and Tangang, 2005; Tangang et al., 2020). The Philippines is considered a separate sub-region due to its vulnerable position at the forefront of climatic events such as typhoons originating in the Pacific Ocean, and a later annual rainfall peak compared to Indochina (Wang and LinHo, 2002; Villafuerte et al., 2014).

Over the ocean, SEA can be classified into different sub-regions, largely independent of the classification over land, based on distinct features such as location, bathymetry, and water mass characteristics. In this study, we conduct the analysis for the entire SEA oceanic region and six specifically determined sub-regions as follows:

- Region 1 (R1): located in the western and northern equatorial part, encompassing part of the Bay of Bengal and Andaman Sea. The region's depth ranges from 500 to 3000 m and its atmospheric conditions are significantly influenced by the southwest summer monsoon.
- Region 2 (R2): bordered by China to the north, Vietnam to the west, the Philippines to the east, and Malaysia to the south. The region's bathymetry varies, with shallow continental shelves around its edges and deeper areas in the central parts, where depths can reach up to 5000 m.
- Region 3 (R3): the Pacific Ocean region east of the Philippines and north of Papua (Indonesia) and Papua New Guinea, encompassing areas such as the Philippine Sea. This region is characterized by deep oceanic trenches near the islands, notably the Philippine Trench, which can reach depths exceeding 10,000 m in some areas, transitioning to vast abyssal plains farther offshore.
- Region 4 (R4): encompasses the Sulu Sea and Celebes Sea lying between the Philippines, Malaysia and Indonesia. The Sulu Sea, in the northwest, features a relatively shallow continental shelf along its edges and a deeper basin in the central part, with depths reaching up to 5000 m. The Celebes Sea, to the southeast, is wider and deeper, with depths exceeding 6000 m in its central area.

Accepted for publication in *Journal of Climate.* DOI 10.1175/JCLI-D-24-0389.1.

R4 serves as a transitional zone for water exchange between R2, R3 and the Indonesian Throughflow (ITF) region (R5).

- Region 5 (R5): also known as the Indonesian Throughflow (ITF) region, connects the Pacific and Indian Oceans through a series of seas and straits within the Indonesian archipelago. The bathymetry of the ITF region is diverse, with a combination of shallow continental shelves (e.g., around 200 to 500 m in the Makassar Strait and Sunda Strait) and deep oceanic basins (e.g., Banda Sea, with depths exceeding 5000 m).
- Region 6 (R6): the oceanic sub-region in the Indian Ocean, south of R1 and located to the south and southwest of the Java Islands. Except for the shallow continental shelves near the coast, the sub-region consists mostly of deeper oceanic areas, including the Sunda Trench located just south of the Java Islands, reaching depths of 7500 m. Warm water from the Pacific Ocean is transported to this sub-region through the ITF region.

The six sub-regions above are linked by key straits, passages, and transition zones (Fig. 1), forming complex passageways between the SEA's interconnected seas, and connecting the Indian and Pacific Oceans (Qu et al., 2005; Sprintall et al., 2019; Trinh et al., 2024).

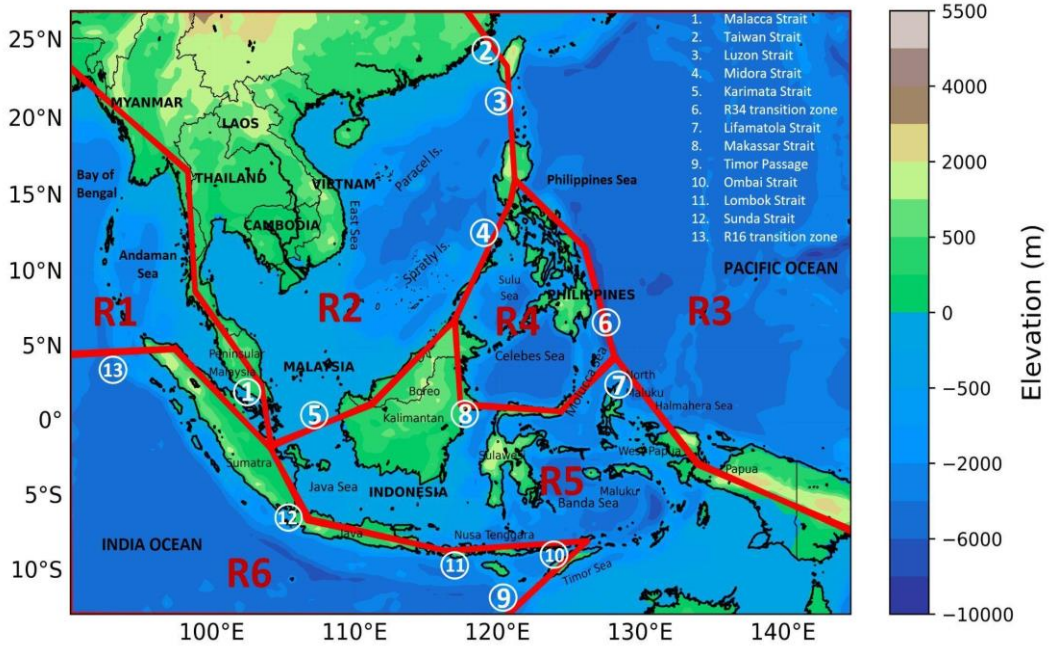

Fig. 1. The Southeast Asia domain. Topography over SEA (shaded) is obtained from the Global 30 Arc-Second Elevation (GTOPO30) dataset (U.S. Geological Survey, 1996).

Accepted for publication in *Journal of Climate*. DOI 10.1175/JCLI-D-24-0389.1.

B. CMIP6 GCMs

We selected 30 CMIP6 GCMs that were accessible at the time of data retrieval (listed in Table 1) to conduct HF estimations on a monthly average basis over SEA. Specifically, we chose the first ensemble member (r1i1p1f1) of the pre-industrial control experiment of each model, and simulations for the future period 2015–2099 under three specific Shared Socioeconomic Pathways (SSPs): SSP1-2.6, SSP2-4.5, and SSP5-8.5 (Riahi et al., 2017).

For comparison purposes, we regridded all model outputs to a common 1°x1° grid using bilinear interpolation. A land-sea mask based on each model's configuration was applied to compute HFs solely over ocean regions.

Model	**Institution / Country**	**Atmospheric horizontal resolutions**	**Model**	**Institution /Country**	**Atmospheric horizontal resolutions**
ACCESS-CM2[4,5,6]	Australia	1.875°x1.25°	FIO-ESM-2-0	China	1.25°x0.9°
ACCESS-ESM1-5[4,5]	Australia	1.875°x1.25°	GFDL-ESM4[1,2,3]	USA	1.125°x1°
BCC-CSM2-MR[1,2,3]	China	1.125°x1.125°	IITM-ESM[1,2,3]	India	1.875°x1.875°
CAMS-CSM1-0[1,2,3]	China	1.125°x1.125°	INM-CM4-8[1,2,3]	Russia	2°x1.5°
CanESM5[4,5,6]	Canada	2.8°x2.8°	INM-CM5-0[1,2,3]	Russia	2°x1.5°
CAS-ESM2-0[4,5]	China	1.4°x1.4°	IPSL-CM6A-LR[6]	France	2.5°x1.3°
CESM2-WACCM[4,5,6]	USA	1.25°x0.9°	KACE-1-0-G[4,5,6]	Korea	1.875°x1.25°
CIESM[5,6]	China	1.25°x0.9°	MIROC6[1,2,3]	Japan	1.4°x1.4°
CMCC-CM2-SR5	Italy	1.25°x0.9°	MPI-ESM 1-2-HR	Germany	0.94 × 0.94°
CMCC-ESM2[4,5]	Italy	1.25°x0.9°	MPI-ESM 1-2-LR[1]	Germany	1.87 × 1.86°
EC-Earth3[4,5,6]	Europe	0.7°x0.7°	MRI-ESM2-0[4]	Japan	1.125°x1.125°
EC-Earth3-Veg[6]	EC-Earth consortium	0.7°x0.7°	NESM3[6]	China	1.875°x1.875°

Accepted for publication in *Journal of Climate*. DOI 10.1175/JCLI-D-24-0389.1.

EC-Earth3-Veg-LR	EC-Earth consortium	1.125°x1.125°	NorESM2-LM[2,3]	Norway	2.5°x1.9°
FGOALS-f3-L[1,2,3]	China	1.25°x1°	NorESM2-MM	Norway	1.25°x0.9°
FGOALS-g3[1,2,3]	China	2°x2°	TaiESM1[4,5,6]	Taiwan	1.25°x0.9°

Table 1. List of CMIP6 GCMs and their respective atmospheric horizontal resolutions used in this study. The superscript next to each model's name indicates the model group, i.e. L or H (defined in sub-section 2.c), to which the model belongs in each specific scenario: [1]L1-2.6, [2]L2-4.5, [3]L5-8.5, [4]H1-2.6, [5]H2-4.5, [6]H5-8.5. Note that most of the models have a horizontal resolution of approximately 100 km for the ocean component, except for CIESM (50 km), GFDL-ESM4 (25 km), MPI-ESM 1-2-HR (50 km), and MPI-ESM 1-2-LR (250 km).

C. REFERENCE DATASETS

The fifth generation of the European Centre for Medium-Range Weather Forecasts (ECMWF) reanalysis, ERA5 (Hersbach et al., 2020), is used as the reference dataset for the HF components. It is important to note that there are currently multiple heat flux datasets, and large disparities may exist among these products (Robertson et al., 2020; Zhang et al., 2023). However, not all datasets cover the entire baseline period 1995–2014 chosen for our present study. Additionally, ERA5 has been demonstrated to provide accurate HF estimates in specific regions worldwide (e.g., Mayer et al., 2023; Pokhrel et al., 2020). Therefore, although ERA5 is selected as the reference dataset, a comprehensive performance assessment of existing heat flux products should be an important topic for future studies.

We used monthly SST data at a 1°x1° resolution from the Hadley Centre Global Sea Ice and Sea Surface Temperature (HadISST) (Rayner et al., 2003) as the reference SST dataset.

D. METHODS

The spatiotemporal characteristics of the CMIP6 multi-model ensemble (MME) HF products are evaluated against ERA5. The MME mean is calculated by averaging the 30 GCMs' results. 1995–2014 is designated as the baseline period of this study. HF projections in the CMIP6 MME are analyzed under three scenarios: SSP1-2.6, SSP2-4.5, and SSP5-8.5, and referred to as MME1-2.6, MME2-4.5, and MME5-8.5, respectively.

Accepted for publication in *Journal of Climate*. DOI 10.1175/JCLI-D-24-0389.1.

Future changes are computed by comparing the mid-century (2041–2060) and end-century (2081–2099) periods with the baseline period.

In the following, a positive (negative) HF corresponds to a gain (loss) of heat for the ocean. A positive HF bias corresponds to an overestimation of heat gain or an underestimation of heat loss (and conversely for a negative bias).

To assess HF sensitivity to future SST rise, we classified the CMIP6 GCMs into two groups based on tercile classification of their projected SST changes (ΔSST): one with the lowest ΔSST values (below the 33rd percentile, referred to as group L) and the other with the highest ΔSST values (above the 67th percentile, referred to as group H). The ΔSST was calculated using the following formula:

$$\Delta SST_{i,j} = \bar{F}(SST)_{i,j} - \bar{H}(SST)_{i,j} \qquad \text{(Eq.1)}$$

where *i* represents an SSP scenario and *j* indicates a specific GCM among the 30 CMIP6 models. $\bar{H}$ and $\bar{F}$ denote the SST means for the SEA region over the baseline period and the future period 2015–2099, respectively.

The ΔSST values vary, ranging from ~0.25ºC for the BCC-CSM2-MR model under SSP1.2-6 to over 2.1ºC for the CanESM5 model under SSP5.8-5 (Fig. 2). With the three SSPs, we obtain six model groups comprising 10 models each: L1-2.6, L2-4.5, L5-8.5, H1-2.6, H2-4.5, and H5-8.5. The models classified into each group are listed in Table 1.

An alternative approach would be to group models based on projected wind changes rather than SST. However, we prioritize SST-based grouping in this study due to its direct impact on HF changes. We acknowledge that a wind-based approach could provide complementary insights into HF sensitivity and represent a promising direction for future research. Furthermore, based on existing literature (e.g. Amaya et al., 2017; Xia et al., 2023), we assume that CMIP6 models generally perform well in simulating SST-wind coupling processes, thus supporting the SST-based classification adopted here. Nonetheless, we recognize the challenges that persist in representing these processes in models (Feng et al. 2023), thereby inducing the need for region-specific evaluations in future work.

To smooth the short-term variability of the data, in the representation of certain figures in the following sections, we employ the locally estimated scatter plot smoothing technique (LOESS) (Cleveland et al., 1988).

Accepted for publication in *Journal of Climate*. DOI 10.1175/JCLI-D-24-0389.1.

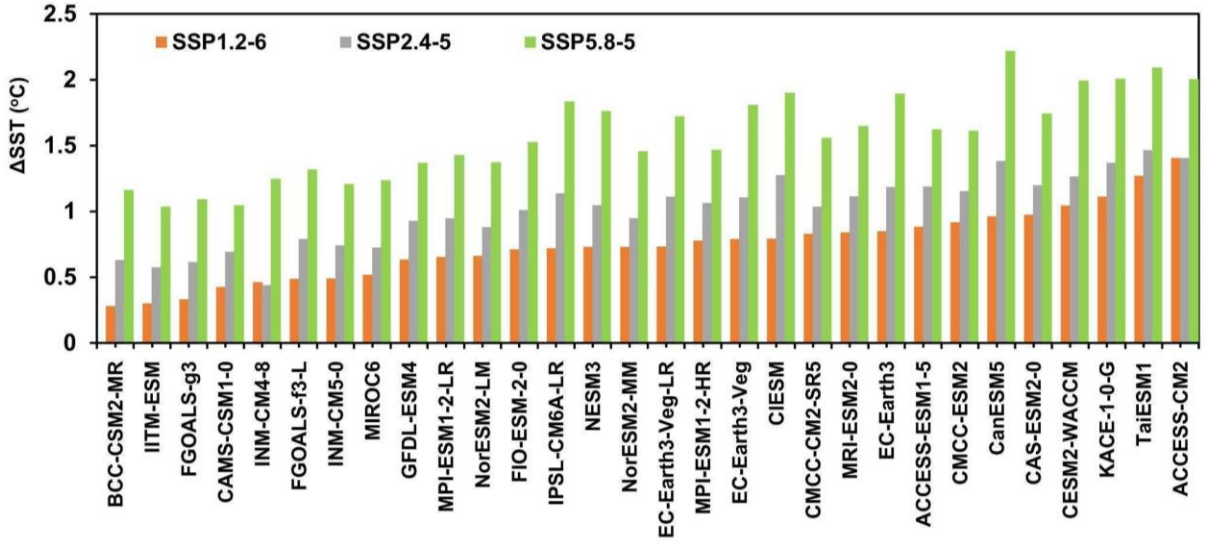

Fig. 2. Projected SST changes over SEA from the 30 CMIP6 models under SSP1.2-6 (orange), SSP2.4-5 (gray), and SSP5.8-5 (green) for the period 2015–2099 relative to the 1995–2014 baseline.

In Section 3.b.3, we investigate the underlying processes that explain the changes in HF components in association with SST changes. We begin with the bulk HF formulae, which are widely used in climate models due to their easy applicability (Large and Yeager, 2004; Yu, 2019):

$$LW = L_d - L_u \quad \text{(Eq.2)}$$

$$LH = \rho L_v C_E W \Delta_z q \quad \text{(Eq.3)}$$

$$SH = \rho C_p C_H W \Delta_z T \quad \text{(Eq.4)}$$

where L_d represents downward longwave radiation flux; $L_u = \epsilon\sigma(SST)^4$ represents upward longwave radiation, with $\sigma = 5.67\text{x}10^{-8}$ $Wm^{-2}K^{-4}$ denotes the Stefan-Boltzmann constant and ϵ represents the surface emissivity, assumed to be 1.0 to account for the small reflected fraction of L_d (Lind and Katsaros, 1986); W represents the 10-m wind speed; $\Delta_z q$ and $\Delta_z T$ represent the differences between 2-m above sea surface and surface values of specific humidity and temperature, respectively; ρ is the air density at the observation level (kg m^{-3}); L_v is the latent heat of vaporization (2.44 × 10^6 J kg^{-1}); C_E and C_H are the transfer coefficients for latent heat and sensible heat, respectively, with values of 1.3×10^{-3} and 0.8×10^{-3} under stable atmospheric conditions (Smith, 1980; Kumar et al., 2017); C_p is the specific heat of air at a constant pressure, assumed to be

Accepted for publication in *Journal of Climate*. DOI 10.1175/JCLI-D-24-0389.1.

constant at 1.005 $\times 10^3$ J $kg^{-1}K^{-1}$.

To examine the dependence of HF changes on SST, we differentiate Eqs. 2–4 with respect to SST to obtain the slope of these relationships, yielding:

$$\frac{\partial LW}{\partial SST} = \frac{\partial L_d}{\partial SST} - 4\epsilon\sigma SST^3 \quad \text{(Eq. 5)}$$

$$\frac{\partial LH}{\partial SST} = \alpha W \frac{\partial \Delta_z q}{\partial SST} + \alpha \Delta_z q \frac{\partial W}{\partial SST} \quad \text{(Eq. 6)}$$

$$\frac{\partial SH}{\partial SST} = \beta W \frac{\partial \Delta_z T}{\partial SST} + \beta \Delta_z T \frac{\partial W}{\partial SST} \quad \text{(Eq. 7)}$$

where $\alpha = \rho L_v C_E$ (Jm^{-3}); $\beta = \rho C_P C_H$ ($Jm^{-3}K^{-1}$).

Eq. 5 indicates the contributions to the LW dependence on SST of longwave radiation directed both downward (first term of the right-hand side) and upward (second term) at the surface. Regarding Eqs. 6 and 7, the first term on the right-hand side represents the thermodynamic contribution, quantifying the impact of humidity and temperature on the LH and SH dependence on SST, respectively. The second term, $\alpha \Delta_z q \frac{\partial W}{\partial SST}$ and $\beta \Delta_z T \frac{\partial W}{\partial SST}$, represents the dynamic contribution, quantifying the influence of wind speed on the LH and SH dependence on SST.

It is worth noting that each CMIP6 model may use a different bulk parameterization, which is beyond the scope of this study to analyze individually. Thus, the parameters used in Eqs. 2–7 represent certain assumptions and may consequently cause imbalances when directly using outputs from the models (Yu, 2019). Therefore, Eqs. 5–7 should be considered approximations rather than exact solutions for estimating the contributions to the HF dependence on SST.

3. Results

A. BASELINE PERIOD: SEASONAL AND SPATIAL VARIABILITY OF HEAT FLUXES

Fig. 3 shows the spatial distribution of annual Qnet and its four components averaged for the baseline period as represented by CMIP6 MME and ERA5. Despite differences in magnitude, the spatial distribution of annual Qnet in the two products exhibits a remarkable similarity with a Pearson spatial correlation coefficient (r) of 0.87. The northern part of the study area has a high annual Qnet loss, while most of the 10ºS–10ºN band shows a Qnet gain. ERA5 estimates the average Qnet over SEA to be 21.3 ± 11.8

Accepted for publication in *Journal of Climate*. DOI 10.1175/JCLI-D-24-0389.1.

Wm^{-2}. CMIP6 MME, with an annual mean value of 6.8 ± 11.4 Wm^{-2}, underestimates the Qnet gain by 14.5 Wm^{-2} (Table 2). Specifically, a significant negative Qnet bias is observed from 10ºN southward.

Among the four HF components, LH exhibits the highest spatial correlation (r=0.88) between CMIP6 MME and ERA5. Both products show significant LH loss, typically ranging from -85 Wm^{-2} to -160 Wm^{-2}, with the largest losses exceeding -190 Wm^{-2} in the western boundary currents around 18ºN–26ºN and 122ºE–125ºE (part of the Kuroshio Current). CMIP6 MME generally overestimates LH loss, especially in the region 10ºS to 10ºN (over the Indonesian Seas). The regional mean annual LH loss overestimation is 11.4 Wm^{-2}.

With values at only about 10% of LH loss, SH loss is relatively small, typically around -10 Wm^{-2}. CMIP6 MME exhibits a moderate spatial correlation (r=0.64) with ERA5 and generally overestimates SH loss. The mean annual SH loss overestimation for the entire region is 1.3 Wm^{-2}.

Regarding SW and LW, CMIP6 MME accurately captures their spatial patterns (with r=0.83 and 0.87, respectively). While there are regions where the models exhibit a positive bias in SW, such as the areas from 90ºE–100ºE and surrounding [5ºS, 140ºE], the annual mean SW bias over the entire region is negative, with a mean underestimation of SW gain of 1.8 Wm^{-2} (Table 2). In terms of LW, the annual mean shows a narrow range (-46 Wm^{-2} to -52 Wm^{-2}) of spatial variability over the region 10ºS–10ºN. Certain areas in the southern hemisphere and the seas near Myanmar (Bay of Bengal) experience significant LW losses (>60 Wm^{-2}). CMIP6 MME exhibits almost no regional mean annual bias in LW (Table 2).

In brief, the 14.5 Wm^{-2} underestimation in annual Qnet gain between CMIP6 MME and ERA5 is primarily due to the overestimation of LH loss (by 11.4 Wm^{-2}), and to a much lesser extent, due to the underestimation of SW gain (by 1.8 Wm^{-2}) and the overestimation of SH loss (by 1.3 Wm^{-2}) in the CMIP6 product.

Accepted for publication in *Journal of Climate.* DOI 10.1175/JCLI-D-24-0389.1.

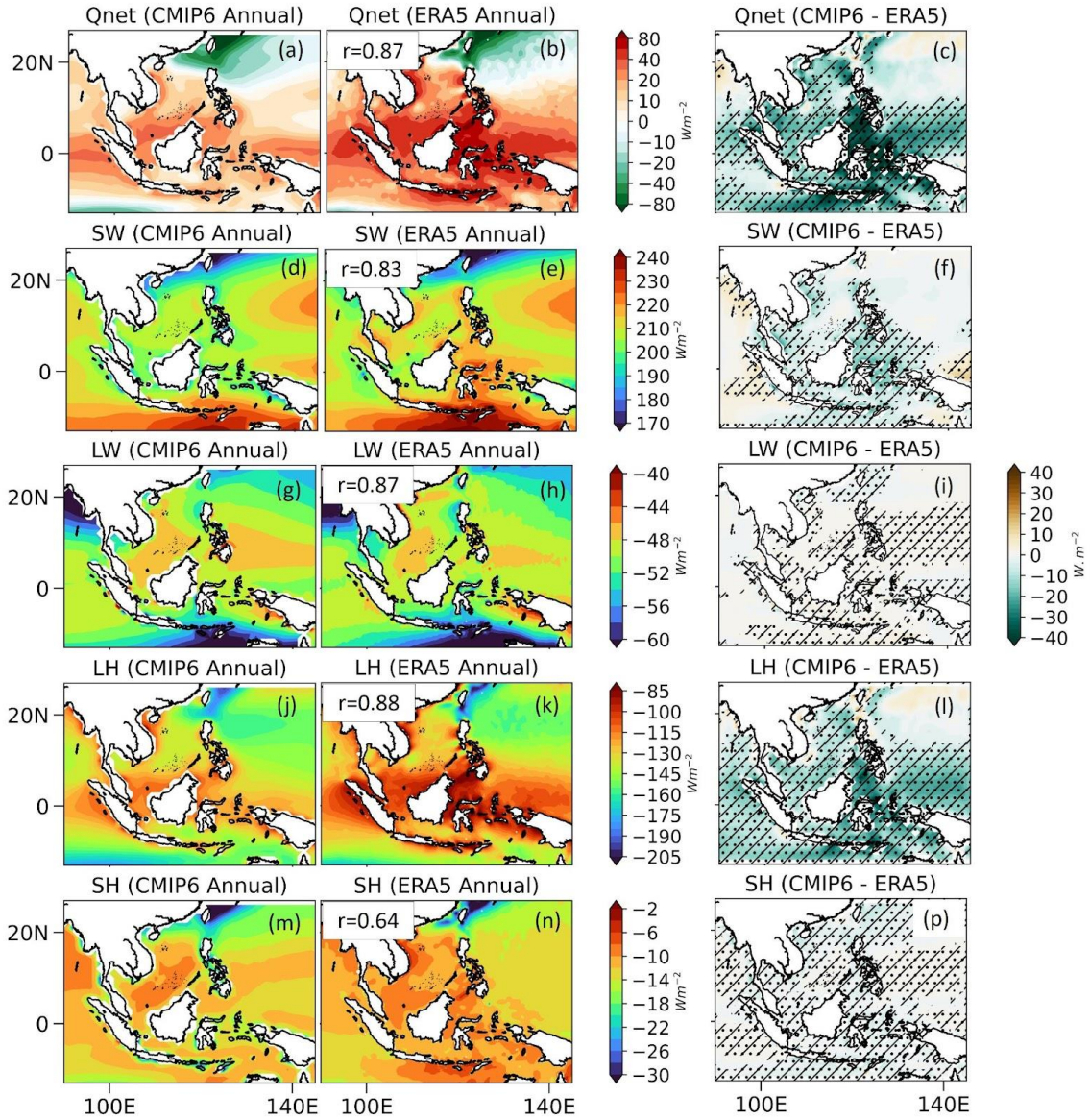

Fig. 3. Annual mean of (a, b) Qnet, (d, e) SW, (g, h) LW, (j, k) LH and (m, n) SH from CMIP6 MME (left) and ERA5 (middle) (Unit: Wm^{-2}). Values in the black boxes of the middle column indicate the Pearson spatial correlation coefficients between ERA5 and CMIP6 MME. Biases between CMIP6 MME and ERA5 are shown in the right column (Unit: Wm^{-2}). The dot-hatch pattern indicates areas where the differences are statistically significant at the 95% confidence level, based on Student's *t*-test.

It is worth noting that Zhang et al. (2018) analyzed the oceanic latent heat flux from the CMIP5 MME product and found a very high spatial correlation coefficient of 0.98 with observations for the global pattern. Zhou et al. (2022), by examining Atmospheric Model Intercomparison Project (AMIP) experiments, which are forced with prescribed SST, demonstrated that AMIP runs from the 6th phase of CMIP (AMIP6) exhibit relatively high correlations over tropical oceans from 30°S to 30°N, with values of 0.94 for LH and 0.75 for SH. In the deep tropics (10°S–10°N), AMIP6 shows outstanding

Accepted for publication in *Journal of Climate*. DOI 10.1175/JCLI-D-24-0389.1.

correlation coefficients of 0.95 for LH and 0.87 for SH. These correlations are higher than the values we obtained in this study with CMIP6 MME for Southeast Asia, which are 0.88 for LH and 0.64 for SH. This is expected, as it is more challenging to capture regional details (refer to Fig. 4 of Zhang et al., 2018). Additionally, the AMIP experiments generally provide better HF values due to their more realistic prescribed SST values. Nevertheless, the spatial correlations shown in Fig. 3 still demonstrate the adequate performance of CMIP6 MME in representing the HF spatial patterns in the region.

The 30 CMIP6 models generally exhibit the same HF spatial patterns to the MME and ERA5 products (Fig. S1–S5). However, some models exhibit strong biases— for example, FGOALS-f3-L and MPI-ESM1-2-HR for SW (Fig. S2), FIO-ESM-2-0 and MIROC6 for LW (Fig. S3), CAS-ESSM2-0 and NEMS3 for LH (Fig. S4), and IITM-ESM and KACE-1-0-G for SH (Fig. S5). Among the 30 CMIP6 models, some tend to overestimate, while others underestimate specific HF components. As a result, the MME products are compensated, bringing the mean values closer to those of the ERA5 reference.

Furthermore, the biases in annual HF values are consistent across seasons (Table 2, Fig. S6). Among the seasons, DJF appears to exhibit the largest biases in all HF components, while JJA shows the least, except for the SW bias in JJA. The biases are statistically significant across most of the SEA oceans, particularly in the ITF region.

Heat fluxes	**Annual**			**DJF**			**MAM**			**JJA**			**SON**		
	CMIP6	ERA5	Bias	CMIP6	ERA5	Bias	CMIP6	ERA5	Bias	CMIP6	ERA5	Bias	CMIP6	ERA5	Bias
Qnet	6.8 ±11.4	21.3 ±11.8	***-14.5***	-31.6 ±16.8	-11.0 ±16.8	***-20.6***	37.0 ±10.7	49.4 ±10.8	***-12.4***	8.3 ± 8.7	20.1 ±8.9	***-11.8***	10.3 ±10.7	27.0 ±11.0	**-16.7**
SW	209.0 ±6.6	210.8 ±7.3	***-1.8***	192.2 ±7.7	195.5 ±9.1	***-3.3***	225.0 ±6.8	226.0 ±7.7	***-1.0***	205.0 ± 5.6	209.3 ±4.5	***-4.3***	210.2 ±7.8	212.5 ±8.1	***-2.3***
LW	*-50.8 ±1.7*	-50.8 ±1.8	***0.0***	-53.1 ±1.9	-51.7 ±2.0	***-1.4***	-51.9 ±1.8	-51.3 ±1.9	***-0.6***	-49.4 ± 1.5	-49.8 ±1.5	***-0.4***	-51.3 ±1.9	-50.9 ±2.0	***-0.4***
LH	*-137.8 ±7.2*	-126.4 ±6.9	***-11.4***	-153.5 ±10.2	-139.8 ±9.2	***-13.7***	-123.9 ±5.8	-114.4 ±5.6	***-8.5***	-135.6 ± 5.9	-128.1 ±6.7	**-7.5**	-135.7 ±5.8	-122.7 ±6.2	***-13.0***
SH	-13.6 ±1.1	-12.3 ±1.1	***-1.3***	-17.2 ±2.0	-15.0 ±1.7	**-2.2**	-12.2 ±1.0	-10.9 ±0.9	***-1.3***	-11.7 ± 0.6	-11.3 ±0.7	***-0.4***	-12.9 ±0.8	-11.9 ±0.9	***-1.0***

Table 2. Annual and seasonal means of Qnet, SW, LW, LH, and SH averaged over SEA along with their respective inter-model standard deviations for CMIP6 MME values and interannual standard deviations for ERA5 (mean ± 1 standard deviation) for the baseline period 1995–2014, as well as the biases of CMIP6 MME compared with ERA5. Units are in Wm^{-2}. A positive (negative) value corresponds to a gain (loss) of heat for the ocean.

Accepted for publication in *Journal of Climate.* DOI 10.1175/JCLI-D-24-0389.1.

To provide a more detailed depiction of the regional specificities of HFs and of their biases, the box plots in Fig. 4 illustrate the distribution of average annual Qnet and its four components across the six sub-regions introduced in Section 2a (R1–R6; refer to Fig. 1), comparing results from the CMIP6 models and ERA5 reanalysis data. In sub-regions such as R1 and R3, large uncertainty ranges in the CMIP6 results can be observed—for example, Qnet, SW, LH, SH in R3, and SW and LW in R1—indicating challenges for models in representing HFs and producing consensual results in these areas. The CMIP6 models generally represent the reference HF values well across the different sub-regions, with some exceptions over R4 and R5, where the models underestimate the Qnet reference values. These underestimated values result from the underestimation of SW in R4, as well as LH and SH in both R4 and R5. Notably, R4 and R5 are located in areas connecting the Pacific and Indian Oceans. Hence, it remains challenging for CMIP6 models to accurately simulate ocean-atmosphere flux exchanges in such regions with complex land topography, islands, and key straits that are poorly represented by coarse-resolution models (see for example Trinh et al. (2024) who highlighted the need for high-resolution studies to correctly capture interocean straits fluxes), thereby inducing biases. This issue deserves further investigation in future studies, possibly using a coupled regional modeling system with higher resolution.

Fig. 5 illustrates the similar latitudinal structures of the zonally averaged annual and seasonal means of Qnet and its four components from CMIP6 MME and ERA5. The annual mean clearly indicates a Qnet gain zone around the equator (i.e., 12ºS–10ºN) and a Qnet loss at higher latitudes. CMIP6 MME consistently underestimates Qnet, with the largest annual bias of approximately -50 Wm^{-2} observed around 2°N. This underestimation could be attributed to the region's strong equatorial dynamics, including, among others, the ITCZ, monsoon systems, equatorial waves, specific warm pools, and the interplay between ocean and atmospheric processes, which are challenging to be fully represented by existing CMIP6 models. Furthermore, certain models operating at relatively coarse resolutions (e.g., 1°x1° or coarser) may be limited in their ability to resolve fine-scale processes that significantly influence HFs in this region.

Accepted for publication in *Journal of Climate.* DOI 10.1175/JCLI-D-24-0389.1.

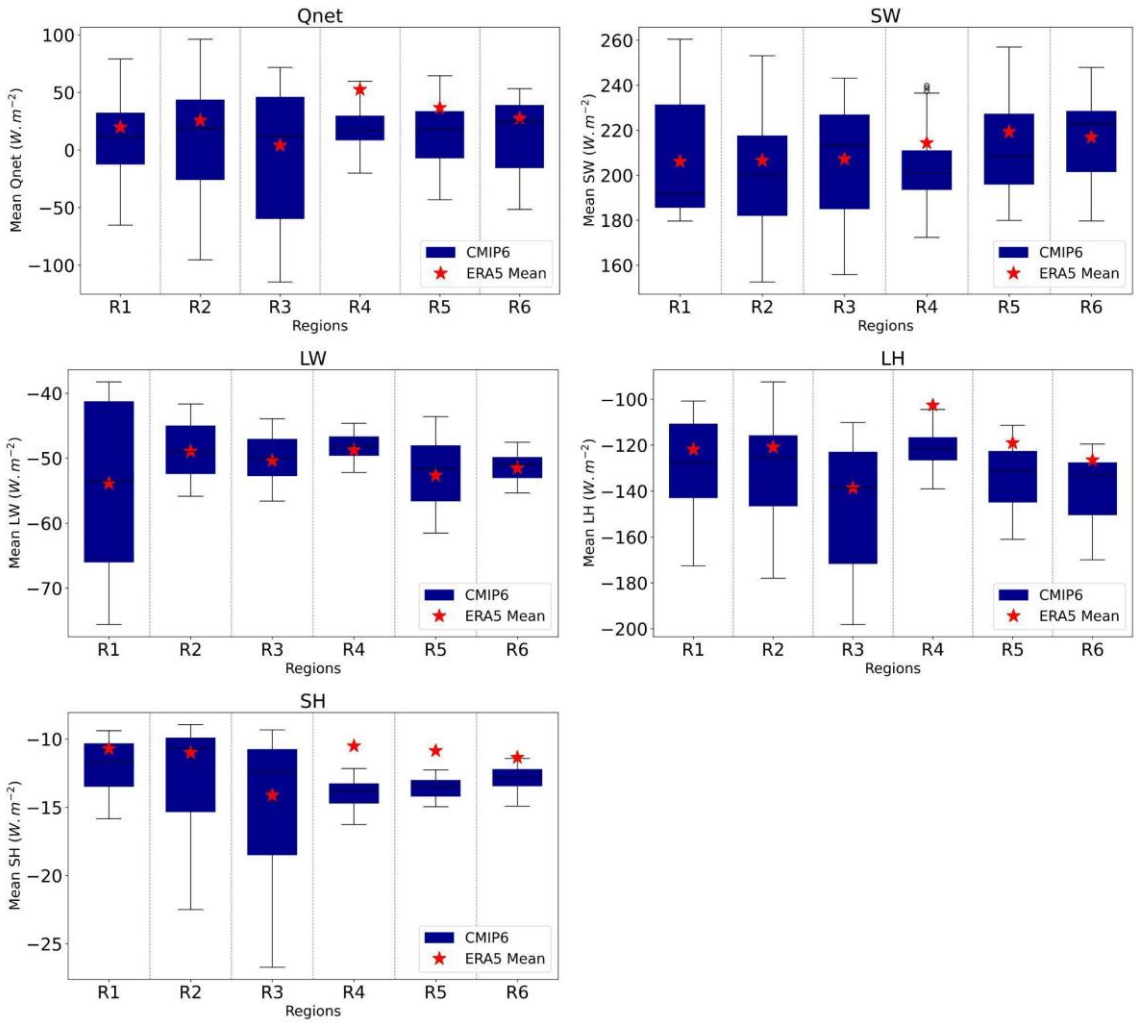

Fig. 4. Box plots of average annual Qnet, SW, LW, LH, and SH over the six sub-regions (R1–R6). The CMIP6 boxes (blue) represent statistics from the 30 models, while the ERA5 values (red star) represent the HF averages during the baseline period.

The annual zonal mean Qnet profile is predominantly depicted by the SW component. CMIP6 MME underestimates SW gain between 0º to 20ºN, with the largest bias of -25 Wm^{-2} also observed around 2ºN. Meanwhile, both LW and SH losses are well represented by CMIP6 MME, exhibiting only minor biases. There is a slight negative (positive) LW bias in the southern (northern) hemisphere and a minor SH bias of approximately -2 Wm^{-2} across the entire latitudinal band. CMIP6 MME overestimates the LH loss, with the maximum overestimation of approximately 15 Wm^{-2} to 20 Wm^{-2} occurring around the equator.

In terms of seasonal variation, Qnet exhibits pronounced variations at different latitudes, excluding the equatorial region. The biases in Qnet of CMIP6 MME compared to ERA5 are noticeable in all seasons, particularly in the region between 10ºS and 10ºN.

Accepted for publication in *Journal of Climate*. DOI 10.1175/JCLI-D-24-0389.1.

SW undergoes the most significant seasonal variation among the HF components, primarily due to its dependence on the seasonal march of the sun. The SW gain underestimation is strongest during DJF, reaching 31 Wm^{-2} around 5ºN, and weaker in other seasons. Meanwhile, LW shows varying biases at each latitude depending on the season, with the largest bias observed during DJF between 5ºN and 20ºN. For LH, strong zonal variations of LH loss are observed during DJF and JJA. The bias of LH loss is the most pronounced compared to other HF components, especially during SON from 10ºN to 10ºS, with LH biases ranging between -30 Wm^{-2} and -20 Wm^{-2}. Finally, the zonal variations of SH are prominently observed during winter in the northern hemisphere, above 20ºN. CMIP6 MME generally exhibits a slight overestimation of SH loss, typically by less than 5 Wm^{-2}, across different seasons and latitudes.

In summary, the zonal mean profile of the HF components during DJF determines their annual profile. SW and LH typically show the most significant latitudinal variations. The substantial variability observed among the models leads to disparities in the estimates of HF components between CMIP6 MME and ERA5. Table 2 quantitatively details that the SEA region experiences a total net heat gain in MAM, JJA and SON, and a total net heat loss in DJF, with the strongest gain observed in MAM. CMIP6 MME consistently exhibits negative biases compared to ERA5 across all seasons and for all HF components. It is of interest to note that the standard deviations of the CMIP6 HF components are comparable to those of ERA5.

Accepted for publication in *Journal of Climate.* DOI 10.1175/JCLI-D-24-0389.1.

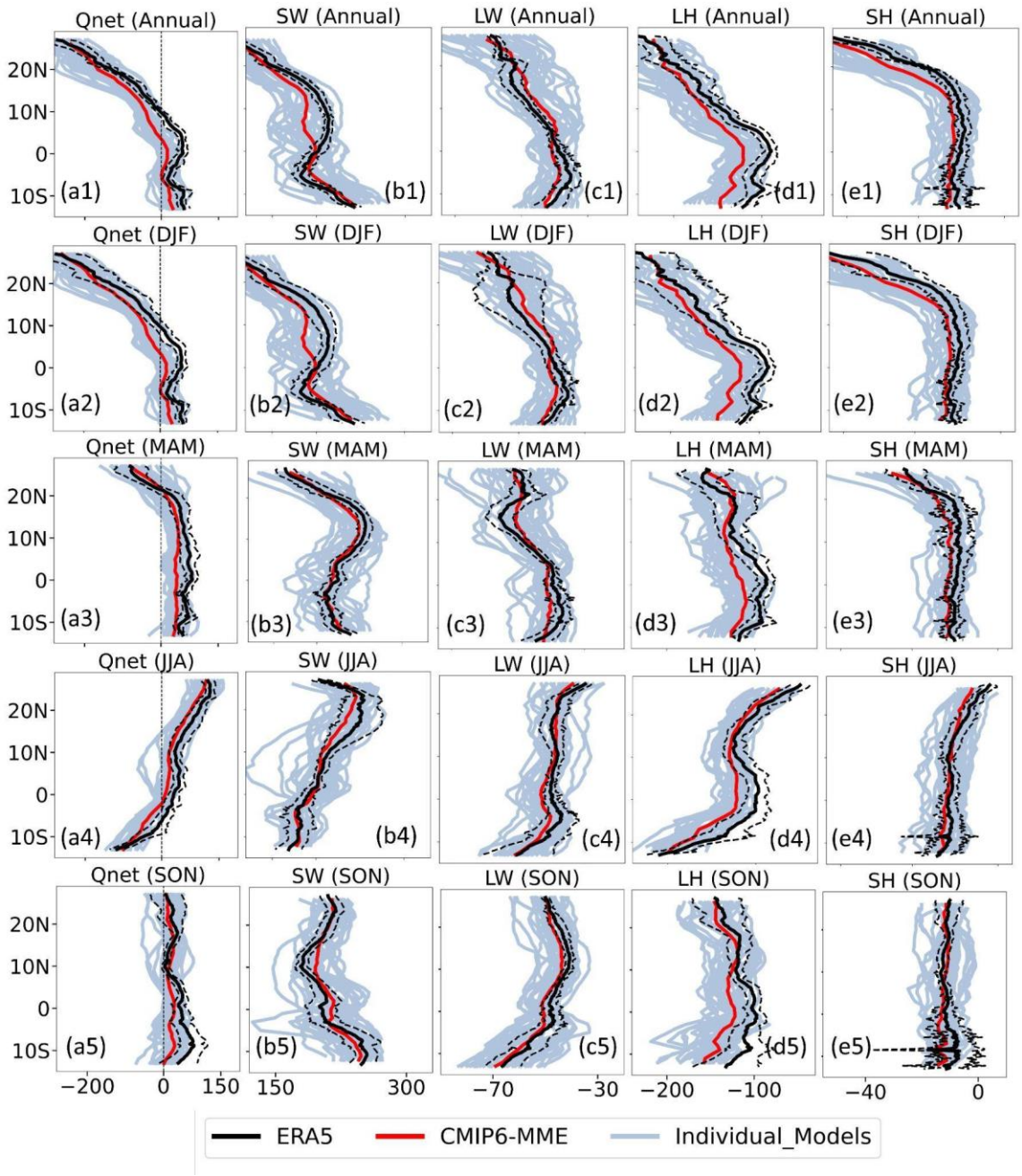

Fig. 5. Zonal mean values (Unit: Wm^{-2}) of Qnet, SW, LW, LH, and SH computed from the annual and seasonal means (December–February, DJF; March–May, MMA; June–August, JJA; September–November, SON) for the baseline period. Red and black lines represent CMIP6 MME and ERA5, respectively. Gray lines indicate the zonal mean profiles of the 30 individual CMIP6 models. Dashed black lines depict the interannual variability in ERA5 based on ±1 standard deviation.

Fig. 6 shows that, despite varying magnitudes, the seasonal cycles of Qnet and its four HF components are generally well represented by the CMIP6 models, with correlations exceeding 0.96 except for LW (r=0.62). The semiannual cycle in Qnet, characterized by its first maximum in April and a second maximum in October, is primarily depicted by SW and LH. The SW peaks observed in April and October

Accepted for publication in *Journal of Climate*. DOI 10.1175/JCLI-D-24-0389.1.

coincide with the times when the Sun crosses the equator. LH also displays a strong semiannual pattern, whereas LW and SH exhibit weaker semiannual cycles.

Consistent with the results discussed above, CMIP6 MME underestimates Qnet compared to ERA5 throughout the year, primarily due to the systematic overestimation of LH loss which exceeds 10 Wm^{-2} for the entire year. CMIP6 MME generally represents the HF components SW, LW and SH in terms of magnitudes. However, notable discrepancies are observed in SH during boreal winter, with differences of up to 3 Wm^{-2}, and in SW and LW from June to September, with differences of up to 4.5 Wm^{-2} for both variables. It is important to note that SW and LW are strongly influenced by cloud radiative effects. Given the frequent occurrence of strong deep convection in SEA, predominantly during June–September (Chen et al., 2000; Wu and Chen, 2021), the notable discrepancies in SW and LW mentioned above could be associated with the large uncertainties of the models in representing convective activities in the region (Ngo-Duc et al., 2017).

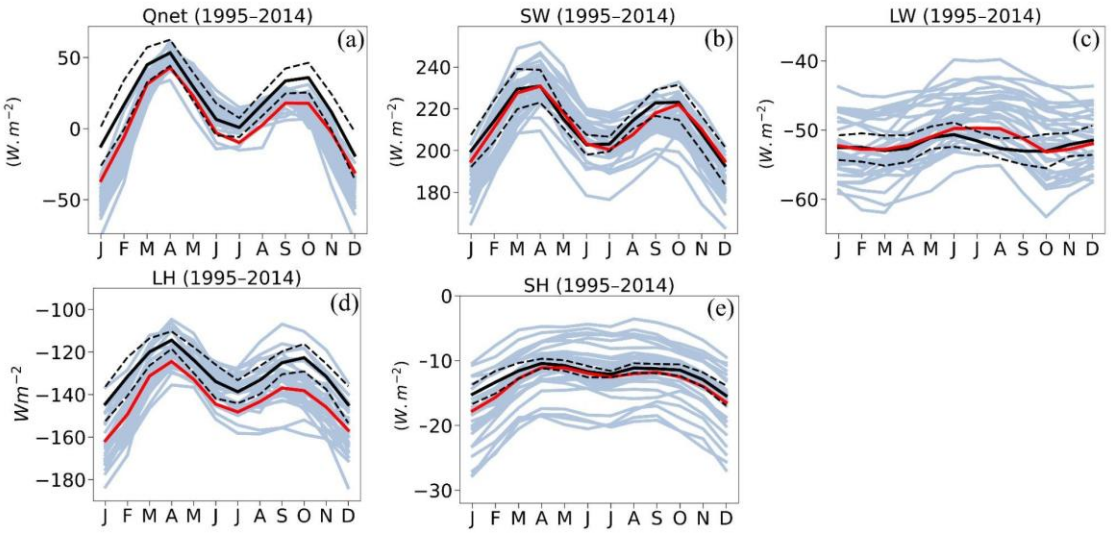

Fig. 6. Seasonal cycle of (a) Qnet, (b) SW, (c) LW, (d) LH, and (e) SH averaged over the SEA region from ERA5 (black line) and CMIP6 MME (red line) for the baseline period (Unit: Wm^{-2}). Gray lines indicate the seasonal cycles of the 30 individual CMIP6 models. Black dashed lines show the range of interannual variability in ERA5 based on ±1 standard deviation. The r values indicate the temporal correlation coefficient between ERA5 and CMIP6 MME (p-value <0.05).

A wide range of performance is observed among individual models within CMIP6 for each HF component. Some models accurately estimate one component but exhibit high inaccuracy with others, resulting in significant discrepancies in Qnet (Table S1). For example, models like INM-CM4-8 and INM-CM5-0 have SW estimates of

Accepted for publication in *Journal of Climate*. DOI 10.1175/JCLI-D-24-0389.1.

approximately 210 Wm^{-2}, which is close to ERA5's 210.8 Wm^{-2}, but they significantly overestimate LH loss (~142 Wm^{-2} compared to ERA5's 126.4 Wm^{-2}). Conversely, models like CAS-ESM2-0 and EC-Earth-Veg underestimate SW (approximately 194.6 Wm^{-2} and 203.9 Wm^{-2}, respectively, compared to ERA5's 210.8 Wm^{-2}), although they have reasonably accurate LH loss estimates compared to ERA5.

B. FUTURE PROJECTIONS

1) Future projections in the multi-model ensemble mean

It is well known that biases remain in CMIP6 simulations, as shown above and in previous research (e.g. Desmet and Ngo-Duc, 2021; Pimonsree et al. 2022; Li et al. 2022; Nguyen-Duy et al. 2024). To date, there exist several approaches to alleviate the influence of model biases in climate projections. The simplest approach is the delta method, assuming that the biases are systematic, i.e. the biases observed during the historical period will persist in future projections (Teutschbein and Seibert, 2012; Jose and Dwarakish, 2022). Therefore, the difference between the future and the baseline period is expected to cancel out the model biases. The second approach involves applying a bias correction method, such as quantile mapping (QM), transfer cumulative probability distribution method (CDF-t), or quantile delta mapping (QDM), to the historical period to derive a transfer function, which can then be applied to future projections (e.g. Guo et al., 2018; Trinh-Tuan et al., 2019; Tong et al. 2020). Using an ensemble of multiple models is another effective way to alleviate biases from individual GCMs, thereby improving the reliability of future climate projections (e.g. Räisänen, 2007; Wang et al., 2023). In our present study, we employ both the delta approach and an ensemble of multiple CMIP6 models to gain insights into future HF changes over the region.

Projected changes in annual HFs over the SEA region based on CMIP6 MME under SSP1-2.6, SSP2-4.5, and SSP5-8.5 scenarios are illustrated in Figs. 7 and 8. In this section, positive (negative) values of changes in HFs (ΔQnet, ΔSW, ΔLW, ΔLH, and ΔSH) indicate an increase (a decrease) of air to sea flux in future periods relative to the baseline period, i.e. an increase of gain for the ocean or a decrease of loss (decrease of gain or increase of loss).

Accepted for publication in *Journal of Climate*. DOI 10.1175/JCLI-D-24-0389.1.

CMIP6 MME projects a general increase in Qnet gain across all examined scenarios for both the mid-century (2041–2060) and end-of-century (2081–2099) periods, relative to the baseline period (Fig. 7). Among the scenarios, SSP5-8.5 exhibits the most substantial increase, while SSP1-2.6 demonstrates the weakest increase for both temporal spans. Specifically, CMIP6 MME projects an average increase of 1, 1.2, and 1.9 Wm^{-2} in annual Qnet on average over the entire SEA for the mid-century under SSP1-2.6, SSP2-4.5, and SSP5-8.5, respectively, and of 0.8, 1.3, and 3.4 Wm^{-2} by the end of the century. These changes show a marked spatial variability, and increases are statistically significant and more prominent south of the Maritime region (around 5ºS, corresponding to the R5 and R6 sub-regions), gradually weakening toward the north. Northern regions around 15ºN over the off-Philippine Sea, in particular R2, R3, and R4, do not exhibit statistically significant changes in the end-century under all scenarios. Although the projected changes for Qnet and its four components (not shown) in the mid-century period are lower than those in the end-century, the spatial patterns remain similar. Therefore, for all subsequent analyses, we focus on the projected changes at the end of the century.

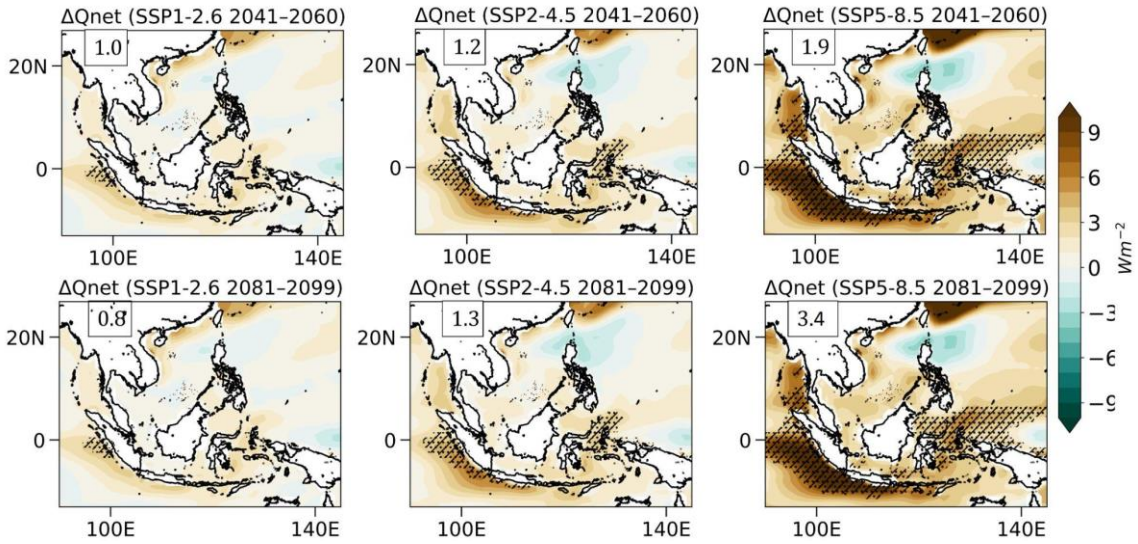

Fig. 7. Projected annual Qnet changes (ΔQnet) from CMIP6 MME under SSP1-2.6 (left), SSP2-4.5 (middle), and SSP5-8.5 (right) for the mid-century (upper panel) and the end-century (lower panel) relative to the baseline period. Shading indicates areas where changes are statistically significant at the 95% confidence level based onStudent's *t*-test. Values in the black boxes show the average projected change in heat flux over the entire region.

Among the four HF components, LH exhibits the most substantial decrease, i.e. an increase of LH loss, of 4.1, 5.4, and 8.4 Wm^{-2} across the entire region under SSP1-2.6,

Accepted for publication in *Journal of Climate*. DOI 10.1175/JCLI-D-24-0389.1.

SSP2-4.5, and SSP5-8.5, respectively, compared to the baseline period (Fig. 8). These changes are particularly pronounced over the central part of the region, between 5°S and 10°N, where the LH loss increase could exceed 10 Wm^{-2} under SSP5-8.5.

The SW gain shows an overall increase throughout the entire region under all scenarios, with the largest (smallest) average increase of 2.9 Wm^{-2} (1 Wm^{-2}) under SSP1-2.6 (SSP5-8.5). The increase is predominantly observed along the southern coast of China, reaching up to 14 Wm^{-2}, 10 Wm^{-2}, and 8 Wm^{-2} under SSP1-2.6, SSP2-4.5, and SSP5-8.5, respectively. Similar to Qnet, SW also exhibits a significant increase in the southwestern Maritime region under all three scenarios, reaching around 5 Wm^{-2} under SSP1-2.6. Meanwhile, a slight SW decrease is projected in the eastern part, close to 142º near the equator and around 15°N, under SSP1-2.6, becoming more pronounced under SSP2-4.5 and further under SSP5-8.5.

Both LW and SH also experience an increase across all scenarios, i.e. a decrease of LW and SH losses. SSP5-8.5 produces the most substantial LW and SH loss weakening of 8.9 Wm^{-2} and 1.9 Wm^{-2} on average over the SEA region, respectively. SSP1-2.6 produces the smallest weakening of 1.8 Wm^{-2} and 0.3 Wm^{-2}, respectively.

Overall, the projected changes in Qnet, LW, LH, and SH are the highest under SSP5-8.5, followed by SSP2-4.5, and the lowest under SSP1-2.6. However, the projected change in SW exhibits an inverse pattern, with the largest change observed under SSP1-2.6 and the smallest change under SSP5-8.5. These contrasting changes in SW could be linked to changes in cloud cover and the associated radiative forcing in the atmosphere and at the surface. For instance, previous studies have demonstrated that clouds exert a positive forcing in both SW and LW in the atmosphere, contributing to atmospheric warming (Ceppi et al., 2017). Concurrently, clouds produce a strong negative SW forcing at the surface during daytime hours and a weakly positive LW forcing, resulting in a cooling effect (Berry and Mace, 2014; Zelinka and Hartmann, 2010). Therefore, the offsetting effects between positive and negative radiative forcing by clouds in SW in the atmosphere and at the surface could account for the opposite changes in SW compared to the other HF components.

Accepted for publication in *Journal of Climate.* DOI 10.1175/JCLI-D-24-0389.1.

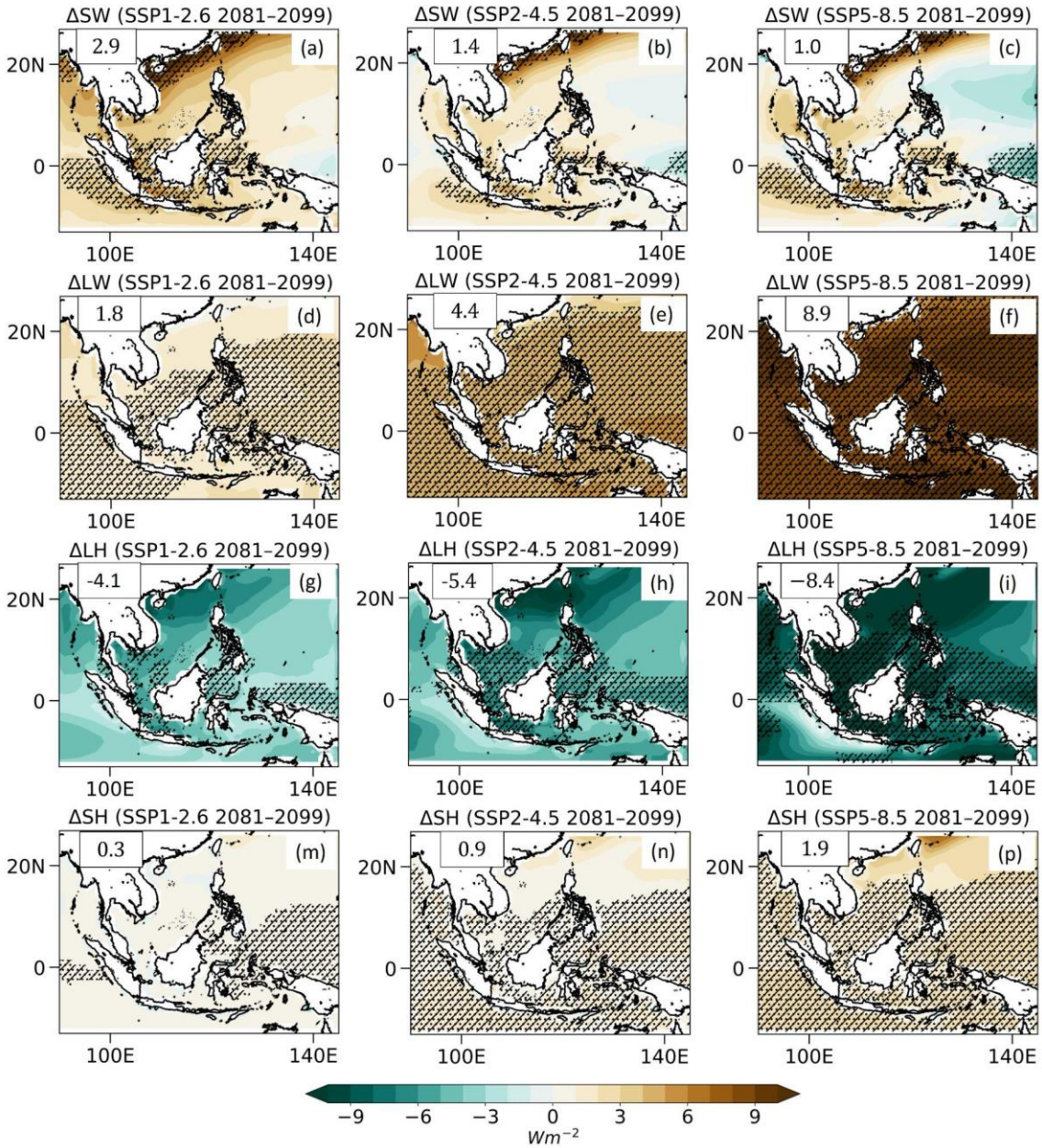

Fig. 8. As in Fig. 7, but for ΔSW, ΔLW, ΔLH, and ΔSH and the end-century only.

2) Future projections in low and high warming groups

Fig. 9 illustrates the sensitivity of HF changes to the warming intensity, including changes for both the low (L1-2.6, L2-4.5, and L5-8.5) and high (H1-2.6, H2-4.5, and H5-8.5) warming model groups, as well as for the CMIP6 multi-model ensemble (MME1-2.6, MME2-4.5, and MME5-8.5).

Overall, Qnet, SW, LW, and SH fluxes are projected to increase, while LH loss exhibits a decreasing trend across all options. Among the scenarios, the most substantial (the least) changes in HFs for both the low and high warming groups are observed under

Accepted for publication in *Journal of Climate*. DOI 10.1175/JCLI-D-24-0389.1.

SSP5-8.5 (SSP1-2.6), with absolute values ranging from 2 to 15 Wm^{-2} (1 to 2 Wm^{-2}) for all components except SW, which is consistent with the MME results discussed in Figs. 7–8.

Within a given scenario, the high warming group consistently projects greater changes in HFs compared to the low warming group, except for SW. Specifically, the H5-8.5 group consistently projects the most substantial changes for Qnet, LH, LW, and SH fluxes, with values of 5, -13, 12, and 3 Wm^{-2}, respectively. In contrast, the L1-2.6 group projects the smallest changes, with values of 1, -2, 2, and 0.1 Wm^{-2}, respectively. Regarding SW, the H1-2.6 group projects the largest change, with an increase of up to 6 Wm^{-2} by the end of the century, followed by the H2-4.5 group and, lastly, the H5-8.5 group. Among the group L models, both the L1-2.6 and L2-4.5 groups show a slight increase in SW, while the L5-8.5 group projects a slight decrease of approximately 1 Wm^{-2} by the end of the century.

It is important to note that the positive trends in Qnet over the SEA oceans were already pronounced during the historical period, indicating that the ocean experienced heat gain, which resulted in observed SST warming during this time (not shown). However, Iskandar et al. (2020), while studying a sub-oceanic region within our study domain—the Indonesian sea—found a significant negative trend in Qnet from 1982 to 2014, favoring a decrease, rather than an increase, in SST. To explain why SST continued to rise in this sub-ocean region despite the decrease in Qnet, they attributed the past increase to upper layer processes, including an increasing trend in precipitation, a decreasing trend in mixed layer depth, the influence of the Indian Ocean Dipole (IOD) and La Niña events, and horizontal heat advection associated with the increasing heat transport from the Pacific to the Indian Ocean via the ITF (R5). To ensure that our results do not contradict those of Iskandar et al. (2020) for the Indonesian sea region, we replotted the Qnet trend for the period 1982–2009—matching the period used in Iskandar et al. (2020)—and found a similar negative Qnet trend over this region (not shown).

Fig. 9b indicates a decreasing trend during the historical period and an increasing trend in the future projections for SW. The SW trend in the historical period corresponds to global dimming, which is well documented in the literature (e.g., Stanhill and Cohen, 2001; Yuan et al., 2021). This dimming phenomenon was partly attributed to increases in

Accepted for publication in *Journal of Climate*. DOI 10.1175/JCLI-D-24-0389.1.

man-made aerosols and other air pollutants, which consequently alter the optical properties of clouds and the atmosphere. Note that dimming occurred up until the early 1990s, followed by a widespread brightening (Wild et al., 2005). Previous studies have demonstrated that CMIP6 models can reproduce the observed regional dimming and brightening in some sub-regions, such as Europe, but perform poorly in other areas, such as China (Moseid et al., 2020). Regarding future trends, the increasing SW trend in Southeast Asia shown in Fig. 9 aligns with results from previous studies. For instance, by analyzing CMIP5 outputs, Wild et al. (2015) attributed this increase to a decrease in cloud cover, allowing SW to reach the surface more easily.

On another note, since ΔLW>0 under global warming (Fig.9c), and $\Delta LW = \Delta L_d - \Delta L_u$ according to Eq.2, we deduce that downward longwave radiation L_d increases more rapidly than upward longwave radiation L_u, i.e. $\Delta L_d > \Delta L_u$. The significant increase in L_d under global warming has been demonstrated in previous studies and is attributed to both atmospheric warming and moistening (Stephens et al., 2012). For instance, the rise in greenhouse gases increases atmospheric temperature, which in turn enhances L_d. Additionally, the positive feedback mechanism resulting from increased atmospheric water vapor due to global warming further amplifies the greenhouse effect and contributes to the increase in L_d. Stephens et al. (2012) also found that clouds contribute to the increase in L_d. Notably, high clouds and low clouds have different impacts on changes in SW and LW (Chen et al., 2000). High clouds can be transparent to SW, while low clouds strongly reflect it; however, both types absorb and emit LW. Consequently, a potential reduction in low cloud coverage, leading to an increase in SW as mentioned above, may still be offset by an increase in high cloud coverage, greenhouse gases, and water vapor feedback in terms of its effect on L_d. This results in a scenario where both SW and L_d increase under global warming.

From a mathematical and experimental perspective, it is known that L_u is closely related to the fourth power of SST (Eq.2). Meanwhile, previous studies have proposed empirical parameterization formulas for L_d, showing that L_d is correlated with the fourth to sixth power of surface temperature (e.g. Dilley and O'Brien, 1998; Stephens et al., 2012). Moreover, Stephens et al. (2012) highlighted the strong performance of the sixth-power relationship. The higher-order dependence of L_d on surface temperature, compared

Accepted for publication in *Journal of Climate*. DOI 10.1175/JCLI-D-24-0389.1.

to that of L_u, explains the more rapid increase in L_d under global warming, as identified above.

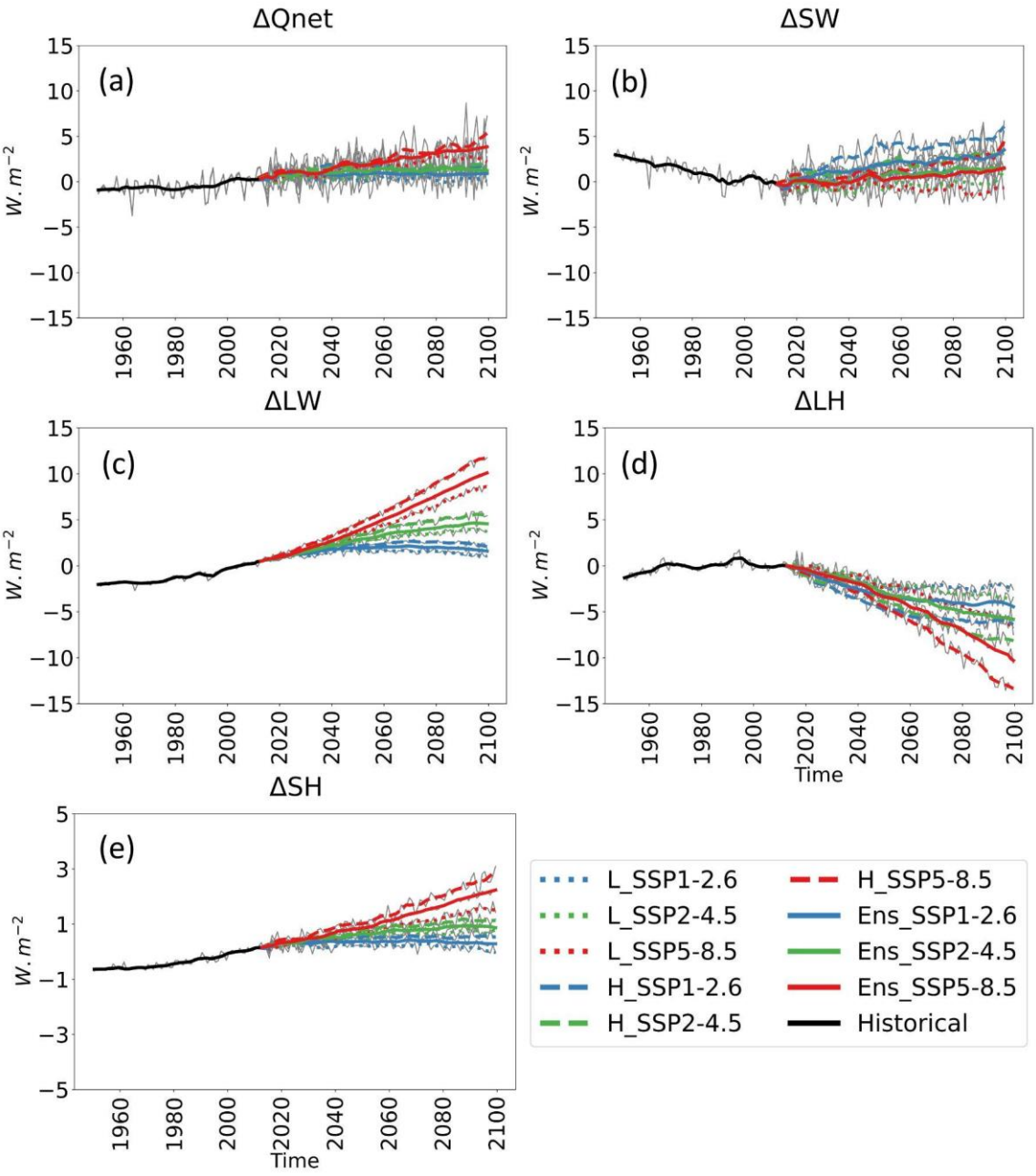

Fig. 9. Time series of projected changes in annual HFs spatially averaged over the study domain relative to the baseline period under SSP1-2.6 (blue), SSP2-4.5 (green), and SSP5-8.5 (red) scenarios for the low warming group (L, dotted line), high warming group (H, dashed line) and the ensemble mean of the 30 CMIP6 models (MME, solid line). Black solid and colored lines, obtained using the LOESS technique, depict historical and future HF anomalies, respectively, while gray lines indicate the ensemble mean values for each group before applying the LOESS technique. Note that the vertical axis limit in Fig. 9(e) differs from those in the other sub-figures to enhance visibility.

Accepted for publication in *Journal of Climate*. DOI 10.1175/JCLI-D-24-0389.1.

3) Relationships between projected HF changes and SST changes

Fig. 10 illustrates the relationships between the average HF changes across the entire SEA region and SST changes within each model group under different scenarios. Both the L and H groups exhibit a similar linear relationship with SST changes, characterized by highly significant (p-value < 0.05) ascending patterns in Qnet, LW, and SH changes with increasing SST, highly significant descending patterns in LH changes, and slight descending patterns in SW changes. Pearson correlation coefficients between HF changes and SST changes exceed the 99% significance test for all HF components except SW. The most significant and positive correlations are observed for Qnet, LW, and SH changes, with values of 0.71, 0.96, and 0.92 for the L group and 0.68, 0.93, and 0.86 for the H group, respectively. LH changes exhibit significant negative correlations with SST increase, at -0.72 for the L group and -0.69 for the H group. Regarding SW, changes with SST increase do not exhibit correlations significant at the 99% level; but the L group shows a more robust correlation (-0.44, p-value <0.05) compared to the H group (-0.12, p-value > 0.05). Consequently, the changes in all HF components except SW show statistically significant linear relationships with SST changes.

Fig. 10 also illustrates the dispersion of individual models' results. The L group displays a smaller dispersion compared to the H group. Among the scenarios, SSP1-2.6 demonstrates the smallest dispersion, followed by SSP2-4.5, with SSP5-8.5 exhibiting the largest dispersion.

Fig. 11, using HF values directly computed and provided by CMIP6 models, shows significant positive and linear correlations between ΔLW and the change of downward longwave radiation flux ΔL_d for both the L and H groups (r_L=0.98 and r_H=0.93) (Fig. 11a). ΔL_d also exhibits strong linear positive correlations with ΔSST (r_L=0.99 and r_H=0.95) (Fig. 11b). Indeed, SST increases lead to higher atmospheric water vapor content, as described by the Clausius-Clapeyron relationship (Held and Soden, 2006). This, in turn, enhances the greenhouse effect, resulting in an increase in downward longwave radiation flux (L_d). Consequently, this raises ΔL_d and, therefore, ΔLW according to Eq. 2. The slope of the linear regression between ΔL_d and ΔSST is approximately 10.2 $Wm^{-2}K^{-1}$ for both the L and H groups (Fig. 11b), corresponding to the first term on the right-hand side of Eq.5. Meanwhile, an increase in ΔSST results in a rise in the upward longwave radiation term at the surface ($4\epsilon\sigma SST^3$ in Eq.5),

Accepted for publication in *Journal of Climate*. DOI 10.1175/JCLI-D-24-0389.1.

contributing to a decrease in ΔLW. With an approximate SST value of 300 K, the term $-4\epsilon\sigma SST^3$ equates to about -6.5 $Wm^{-2}K^{-1}$. Consequently, we obtain for Eq.5: $\frac{\partial LW}{\partial SST} = 10.2 - 6.5 = 3.7$ ($Wm^{-2}K^{-1}$), in agreement with the slope of the linear regression line between ΔLW and ΔSST (respectively 3.69 and 3.72 $Wm^{-2}K^{-1}$ for the L and H groups, Fig. 10c). The reduction in LW loss from the ocean, i.e., the increase in LW flux, is therefore driven both directly by the increase in SST and indirectly by its effect on L_d, which acts in opposition to the direct effect.

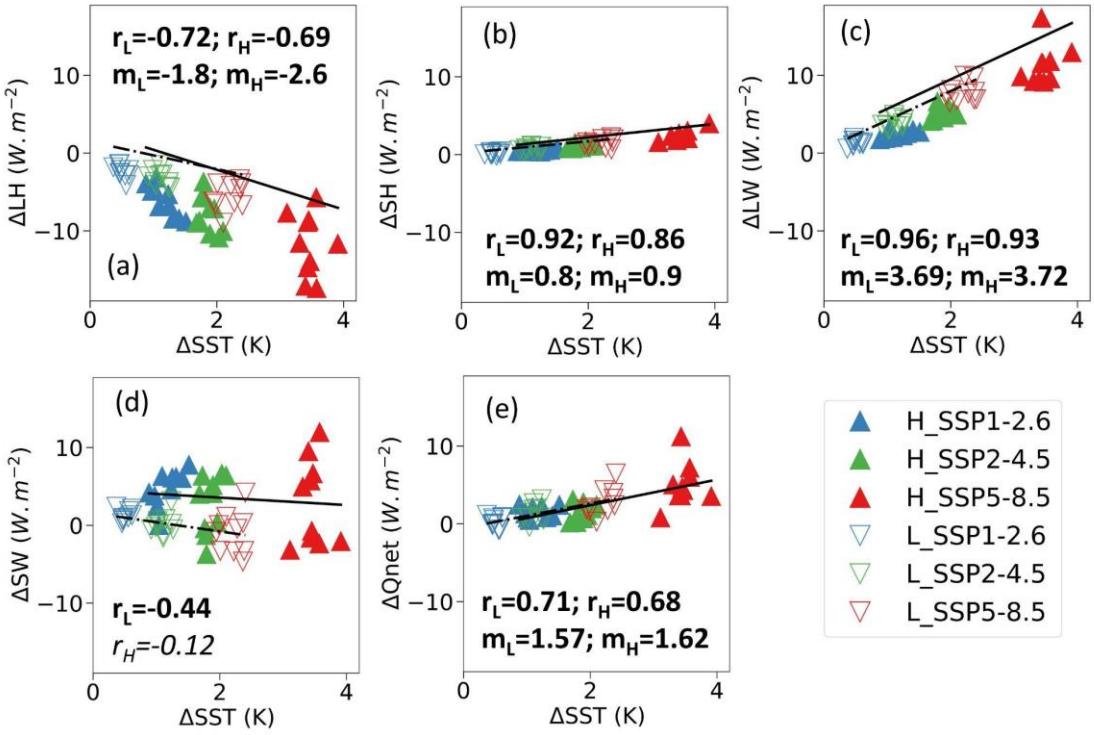

Fig. 10. Projected changes in Qnet and its four components versus changes in SST by the end of the century relative to the baseline period. Filled upward-pointing triangles represent the high warming (H) group, while non-filled downward-pointing triangles represent the low warming (L) group. Blue, green, and red colors correspond to the scenarios SSP1-2.6, SSP2-4.5, and SSP5-8.5, respectively. Solid and dash-dotted lines represent linear regressions for the H group and the L group, respectively. Pearson correlation coefficients between ΔSST and changes for the L group and H group are denoted as r_L and r_H, respectively. Bold values indicate p-value <0.05 and italic values indicate p-value >0.05. Values of m_L and m_H are slopes for components showing a highly statistically significant linear relationship (p-value <0.01) for groups L and H, respectively.

Fig. 11c illustrates weak and non-significant negative correlations between the change of wind speed ΔW and ΔSST. The slopes of the trend lines are negligible, with values of -0.01 and -0.008 $ms^{-1}K^{-1}$ for the L and H groups, respectively. This suggests that the 10-m wind speed does not change significantly with sea surface warming, and

Accepted for publication in *Journal of Climate*. DOI 10.1175/JCLI-D-24-0389.1.

that the dynamic term in Eqs. 6 and 7 does not substantially contribute to the relationship between changes in LH and SH with respect to changes in SST. This finding is supported by the weak and non-significant correlations between ΔLH and ΔW (Fig. 11d) and between ΔSH and ΔW (Fig. 11e).

Hence, changes in LH and SH with respect to changes in SST are primarily driven by the thermodynamic term, which accounts for the contributions of changes in the specific humidity and temperature differences between 2-m above sea surface and surface, $\Delta_z q$ and $\Delta_z T$, respectively. Fig. 11f illustrates negative linear relationships between $\Delta(\Delta_z q)$ and ΔSST with correlation coefficients r_L=-0.62 and r_H=-0.73, and slopes (i.e. $\frac{\partial \Delta_z q}{\partial SST}$ values) of -0.48 and -0.36 g.kg^{-1}K^{-1} for the L and H groups, respectively. The regional-mean W values computed during the period 2081–2099 across the three scenarios are 1.6 and 3.1 ms^{-1} for the L and H groups, respectively. Therefore, the thermodynamic term in Eq. 6, i.e. $\alpha W \frac{\partial \Delta_z q}{\partial SST}$, amounts to approximately -1.8 and -2.7 Wm^{-2}K^{-1} for the L and H groups, respectively. These values are in agreement with the slope values obtained from the linear regression between ΔLH and ΔSST in Fig. 10a (-1.8 and -2.6 Wm^{-2}K^{-1}, respectively). In brief, the mechanism can be explained by the fact that warmer SSTs increase the saturated specific humidity over the ocean, as described by the Clausius-Clapeyron relationship. Consequently, the difference between the actual water vapor content in the air and its saturation capacity is amplified. This increased difference drives stronger evaporation from the ocean surface, leading to increased LH loss (Zhang and Mcphaden, 1995; Kumar et al., 2017).

Fig. 11g depicts a positive linear relationship between $\Delta(\Delta_z T)$ and ΔSST, with correlation coefficients r_L=0.8 and r_H=0.78, and slopes of 0.40 and 0.38 K.K^{-1} for the L and H groups, respectively. The thermodynamic term of Eq. 7, i.e. $\beta W \frac{\partial \Delta_z T}{\partial SST}$, amounts to approximately 0.75 and 1.1 Wm^{-2}K^{-1} for the L and H groups, respectively, which is close to the slope values obtained from the linear regression between ΔSH and ΔSST (0.8 and 0.9 Wm^{-2}K^{-1}, respectively, Fig. 10b). Therefore, the magnitude of SH increase, i.e. SH loss decrease, is primarily driven by the temperature difference between the ocean surface and the overlying air layer. As SST increases, the emission of longwave radiation from the ocean rises significantly, as described by the Stefan-Boltzmann law. This release of longwave radiation into the atmosphere warms the adjacent air layers,

Accepted for publication in *Journal of Climate*. DOI 10.1175/JCLI-D-24-0389.1.

particularly when the atmosphere has high humidity. As a result, the additional warming at the sea surface reduces the temperature difference between the surface and the near-surface air (i.e., it inversely increases the changes in $\Delta_z T$, as shown in Fig. 11g), thereby decreasing SH loss (Thum et al. 2002; Wu and Zhang, 2024).

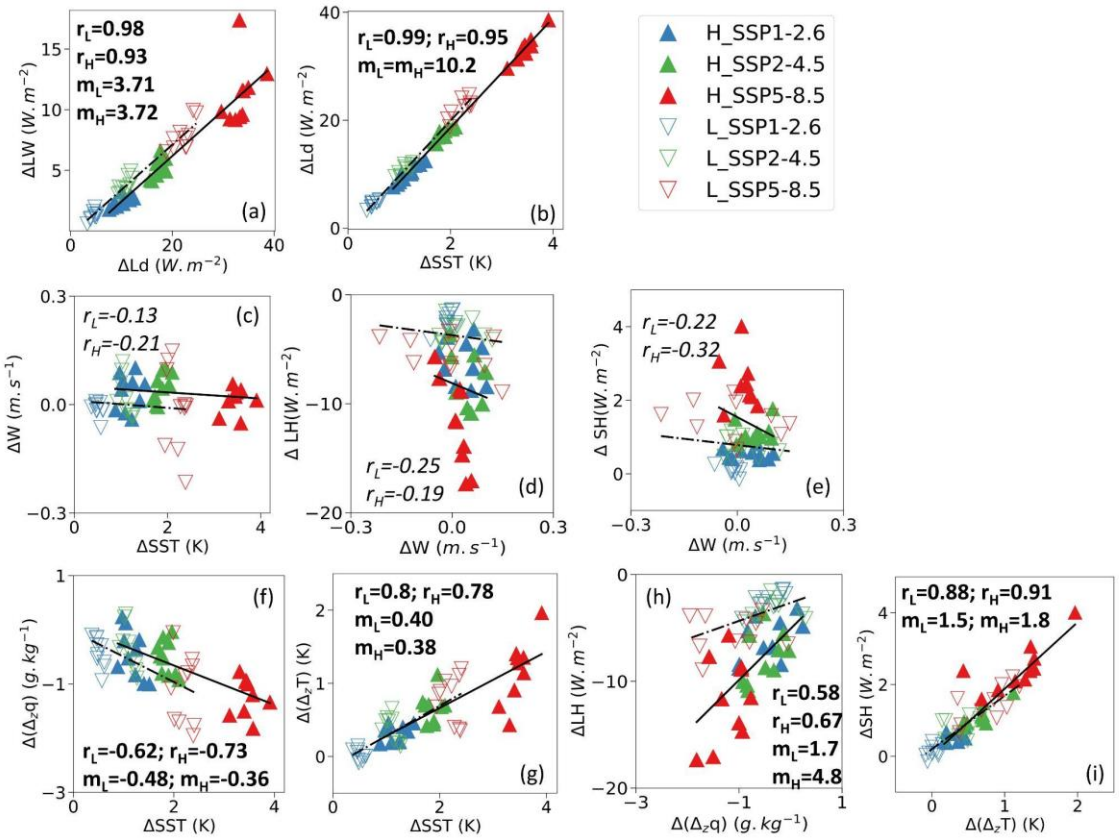

Fig. 11. As in Fig. 10, but for projected changes in (a) LW versus L_d, (b) L_d versus SST, (c) W versus SST, (d) LH versus W, (e) SH versus W, (f) $\Delta_z q$ versus SST, (g) $\Delta_z T$ versus SST, (h) LH versus $\Delta_z q$, and (i) SH versus $\Delta_z T$.

4. Conclusions

In this study, we first examined the representation of air-sea HFs over the SEA region using data from 30 CMIP6 GCMs compared with ERA5 reanalysis for the baseline period 1995–2014. Both CMIP6 MME and ERA5 indicate a net heat gain for the ocean in the region (with mean values of respectively 6.8±11.4 Wm^{-2} and 21.3±11.8 Wm^{-2}, respectively), although CMIP6 MME underestimates Qnet, primarily due to an overestimation of LH loss. There is a high spatial similarity in Qnet between CMIP6 MME and ERA5, with a correlation of 0.87 for the annual average. The zonal average of Qnet in CMIP6 MME is consistently lower than that in ERA5, with the largest biases occurring during the DJF season and the smallest biases during MAM. These differences

Accepted for publication in *Journal of Climate*. DOI 10.1175/JCLI-D-24-0389.1.

are primarily attributed to the biases observed in LH and SW. Notably, CMIP6 MME successfully captures the seasonal cycle of all components of air-sea HFs over the SEA region. The semiannual cycle of Qnet is well depicted, with primary peaks in April and October, mainly attributable to the seasonal variations in LH and SW.

The projected air-sea HFs were then investigated, revealing consistent increases in Qnet gain across all CMIP6 models. These increases are pronounced at the mid-century and intensified further by the end of the century under all scenarios, particularly under SSP5-8.5. The model group projecting higher SST increases demonstrates a more pronounced linear trend in HFs, except for SW. The projected changes in Qnet in relation to the changes in SST are primarily attributable to the changes in LW, LH, and SH. There is a decrease in LW loss when SST increases, driven by enhanced downward longwave radiation, though this is partially offset by an increase in upward longwave radiation. The LH loss increase, and SH loss decrease with increasing SST are associated with the thermodynamic effect, which changes linearly with SST, rather than with the dynamic effect, which does show a significant trend with sea surface warming.

In numerical modeling, air-sea HFs are commonly estimated using bulk formulae (Bonino et al., 2022). However, uncertainties in the parameterizations of these bulk formulae can introduce significant biases into HF estimates (Wang et al., 2017; Weare, 1989; Zhou et al., 2020). Addressing these biases in CMIP models for the Southeast Asia region remains a critical area for future research. Moreover, sensible heat flux due to rainfall, which can be significant in the tropics (e.g., Ramos et al. 2021; Ibrahim and Sun 2023; Zhou et al. 2024a,b), is typically ignored in climate models. Given the region's abundant rainfall, incorporating this component alongside the four main HF components, would provide a more comprehensive understanding of the HF budget in Southeast Asia. Finally, it is noteworthy that all model outputs in this study were regridded to a common 1°×1° grid—a relatively coarse resolution—to facilitate comparison. Further studies using higher-resolution simulations, such as those available through the CORDEX-SEA program, could effectively improve regional climate assessments.

Acknowledgments.

This work is supported by the Vietnam National Foundation for Science and Technology Development (NAFOSTED, Vietnam) under Grant 105.06-2021.14, by the LOTUS international joint laboratory funded by the French National Research Institute

Accepted for publication in *Journal of Climate.* DOI 10.1175/JCLI-D-24-0389.1.

for Sustainable Development (IRD, France), and by the SEASTERS project funded by the Centre National d'Etudes Spatiales (CNES, France) TOSCA program. Hue Nguyen-Thanh's Ph.D. thesis is partly supported by the French Embassy in Vietnam via the Scholarship of Excellence.

Data Availability Statement.

The CMIP6 model data were downloaded from the ESGF nodes: https://esgf.llnl.gov/nodes.html. The ERA5 data are available at: https://www.ecmwf.int/en/forecasts/dataset/ecmwf-reanalysis-v5; and the HadISST data at https://rda.ucar.edu/datasets/ds277.3.

Accepted for publication in *Journal of Climate*. DOI 10.1175/JCLI-D-24-0389.1.

APPENDIX

Table S1. Annual means of HF components ($W.m^{-2}$) and SST (ºC) for each CMIP6 model, averaged over SEA for the historical period.

		Historical					
No.	**Models**	**SW**	**LW**	**LH**	**SH**	**Qnet**	**SST**
1	ACCESS-CM2	212.4	-50.4	-151.6	-8.5	1.9	28.6
2	ACCESS-ESM1-5	220.7	-50.5	-153.8	-8.3	8.1	28.9
3	BCC-CSM2-MR	216.3	-51.9	-147.6	-9.2	7.7	29.1
4	CAMS-CSM1-0	207.9	-54.2	-136.7	-11.2	5.8	28.3
5	CanESM5	208.2	-49.1	-138.3	-13.3	7.4	28.9
6	CAS-ESM2-0	194.6	-48.4	-125.8	-9.3	11.2	28.3
7	CESM2-WACCM	206.1	-47.6	-135.8	-13.2	9.5	29.0
8	CIESM	209.4	-45.5	-143.2	-11.0	9.6	28.5
9	CMCC-CM2-SR5	206.7	-45.7	-143.6	-12.3	5.1	29.0
10	CMCC-ESM2	209.2	-46.3	-144.8	-12.1	6.0	28.8
11	EC-Earth3	204.3	-54.6	-129.1	-13.6	6.9	28.1
12	EC-Earth3-Veg	203.9	-54.3	-128.7	-13.6	7.3	28.2
13	EC-Earth3-Veg-LR	201.0	-55.3	-125.5	-13.7	6.5	27.6
14	FGOALS-f3-L	223.1	-51.6	-147.1	-17.0	7.5	27.8
15	FGOALS-g3	218.0	-55.8	-140.2	-13.6	8.4	28.5
16	FIO-ESM-2-0	202.8	-43.8	-137.4	-12.5	9.2	28.1
17	GFDL-ESM4	206.6	-54.9	-134.5	-12.6	4.6	28.1
18	IITM-ESM	206.0	-58.6	-136.7	-5.9	4.7	26.9
19	INM-CM4-8	211.7	-50.8	-142.7	-12.6	5.6	28.2
20	INM-CM5-0	209.7	-51.2	-144.5	-12.5	1.5	27.7
21	IPSL-CM6A-LR	207.0	-52.0	-138.5	-14.8	1.7	28.3
22	KACE-1-0-G	217.5	-52.0	-144.3	-8.1	13.0	28.4
23	MIROC6	192.6	-44.2	-140.8	-7.4	0.2	28.1
24	MPI-ESM1-2-HR	225.4	-54.7	-138.7	-20.0	12.1	27.8
25	MPI-ESM1-2-LR	220.7	-53.1	-138.3	-21.3	8.0	27.4
26	MRI-ESM2-0	212.2	-51.9	-134.2	-11.4	14.7	28.1
27	NESM3	192.9	-46.5	-121.1	-19.8	5.5	27.3
28	NorESM2-LM	205.0	-47.7	-140.2	-15.0	2.1	29.1
29	NorESM2-MM	208.6	-50.3	-138.9	-14.9	4.5	28.9
30	TaiESM1	206.3	-46.9	-140.7	-11.6	7.1	28.4

Accepted for publication in *Journal of Climate*. DOI 10.1175/JCLI-D-24-0389.1.

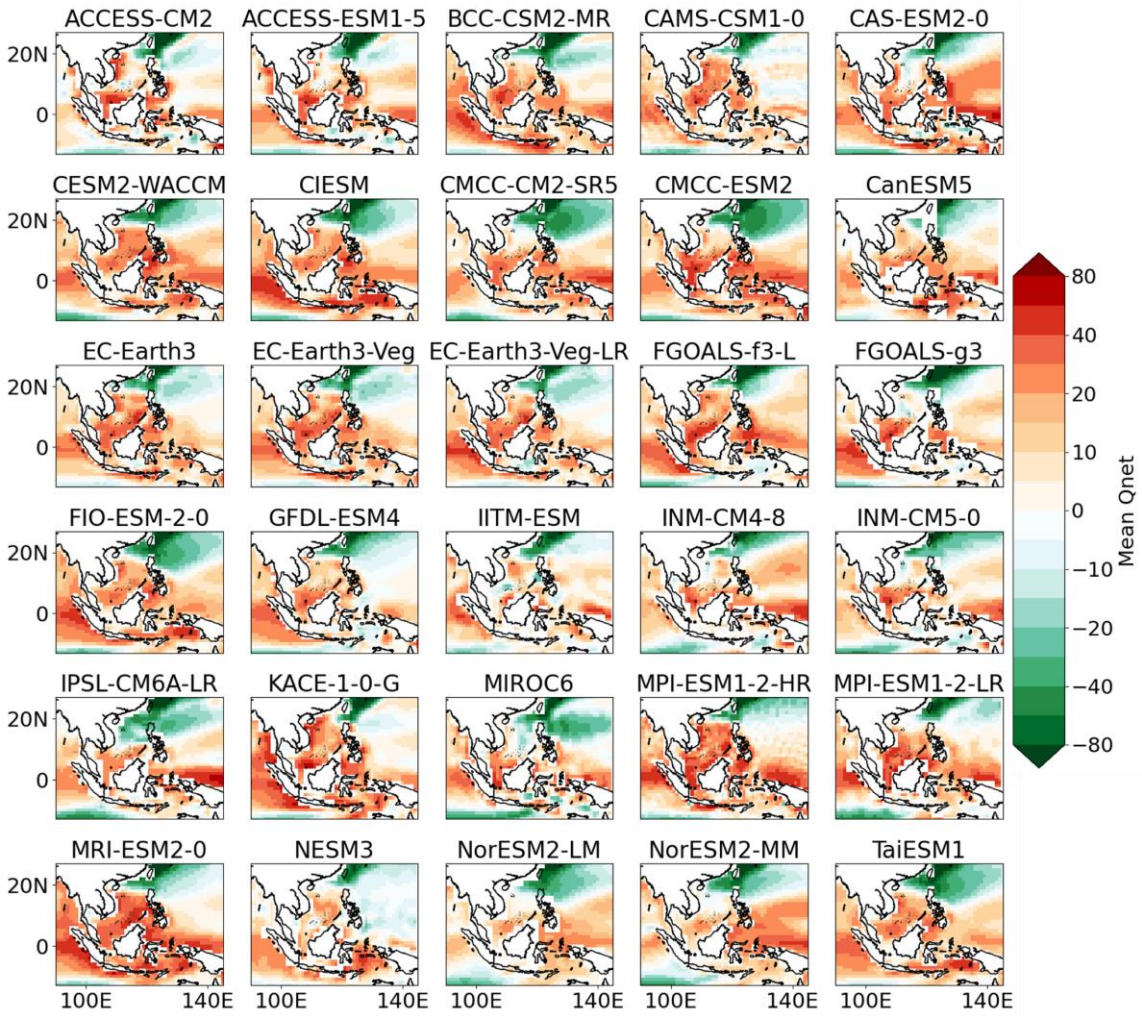

Fig. S1. Annual mean of Qnet during the baseline period for 30 individual models from CMIP6 (Unit: Wm^{-2}).

Accepted for publication in *Journal of Climate*. DOI 10.1175/JCLI-D-24-0389.1.

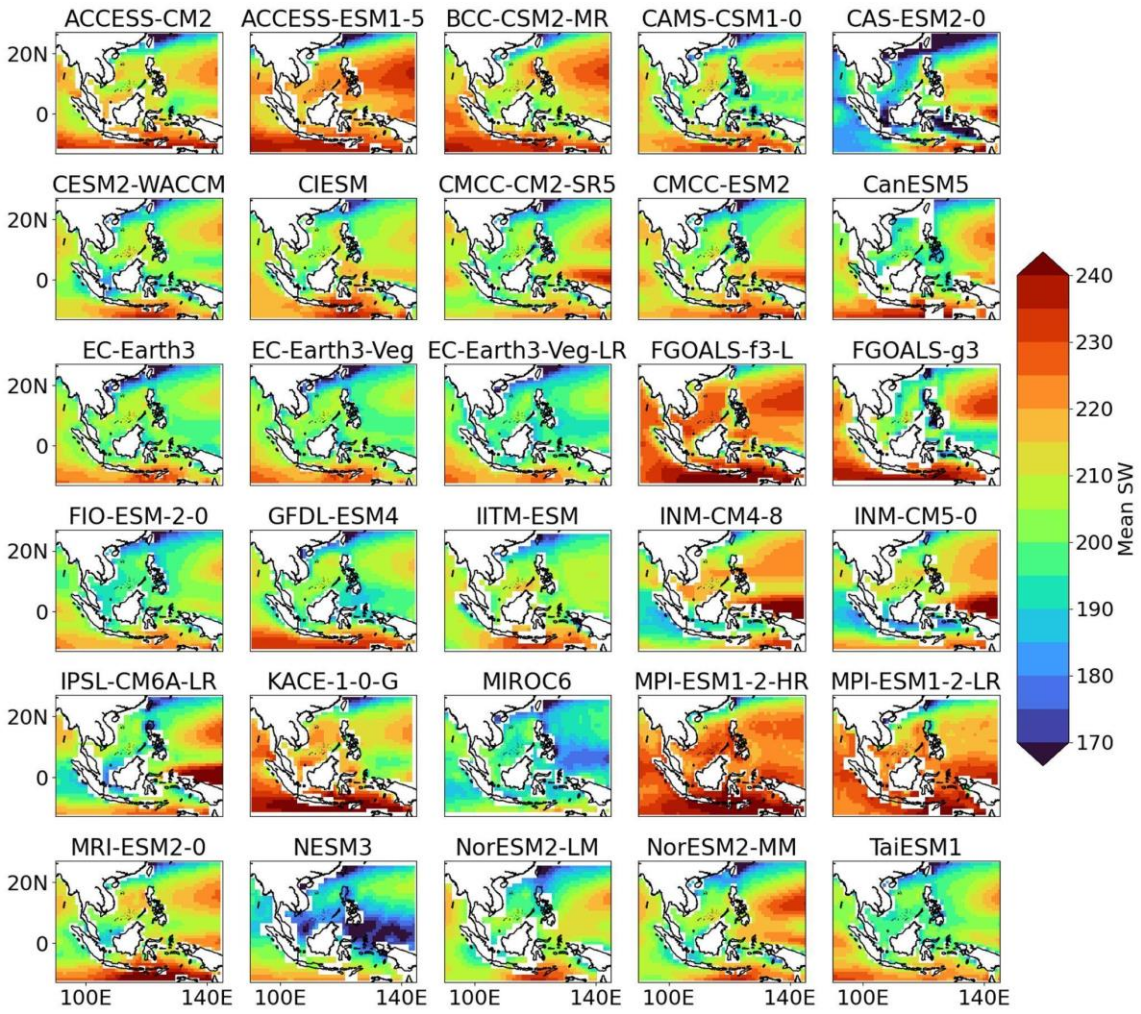

Fig. S2. As in Fig. S1, but for SW.

Accepted for publication in *Journal of Climate*. DOI 10.1175/JCLI-D-24-0389.1.

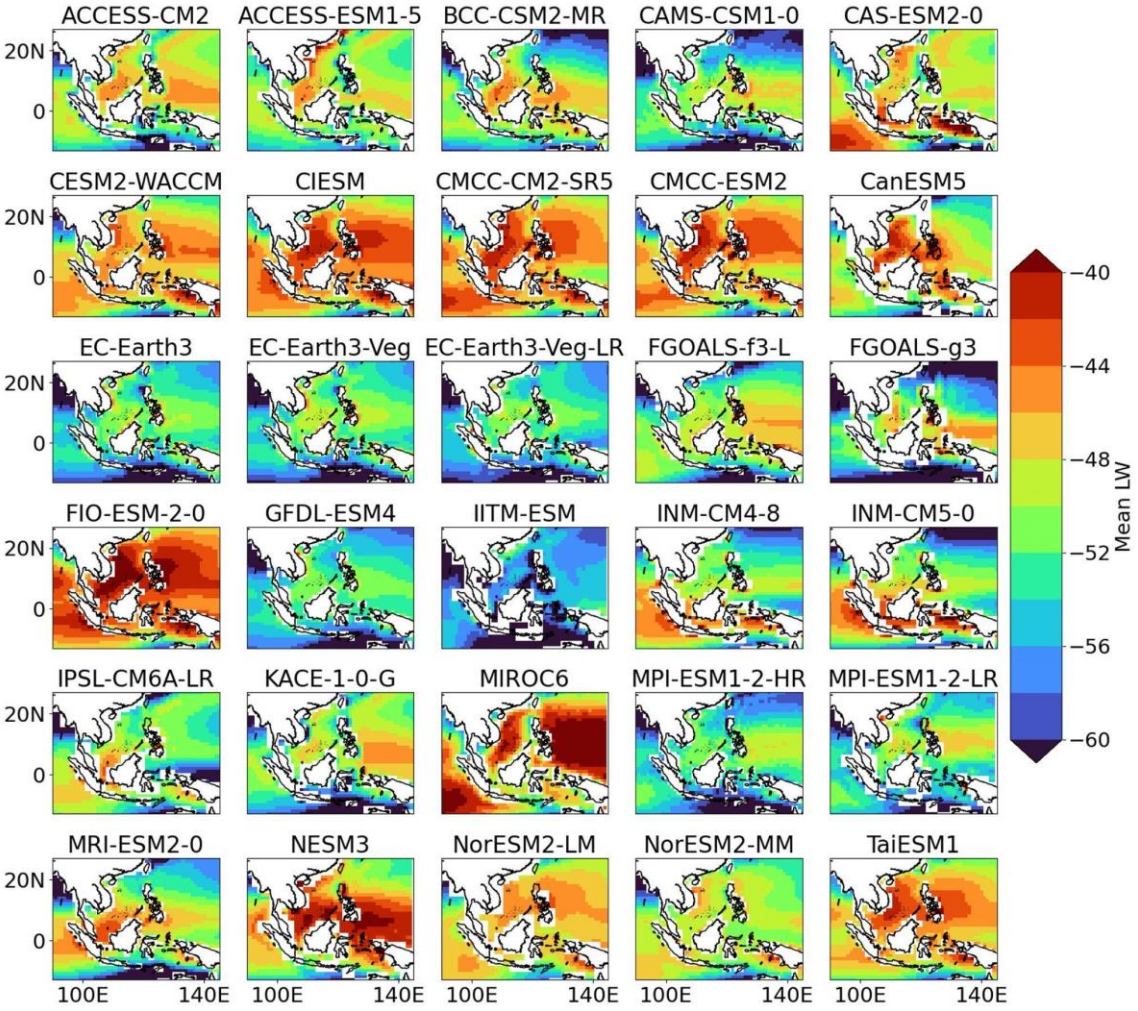

Fig. S3. As in Fig. S1, but for LW.

Accepted for publication in *Journal of Climate*. DOI 10.1175/JCLI-D-24-0389.1.

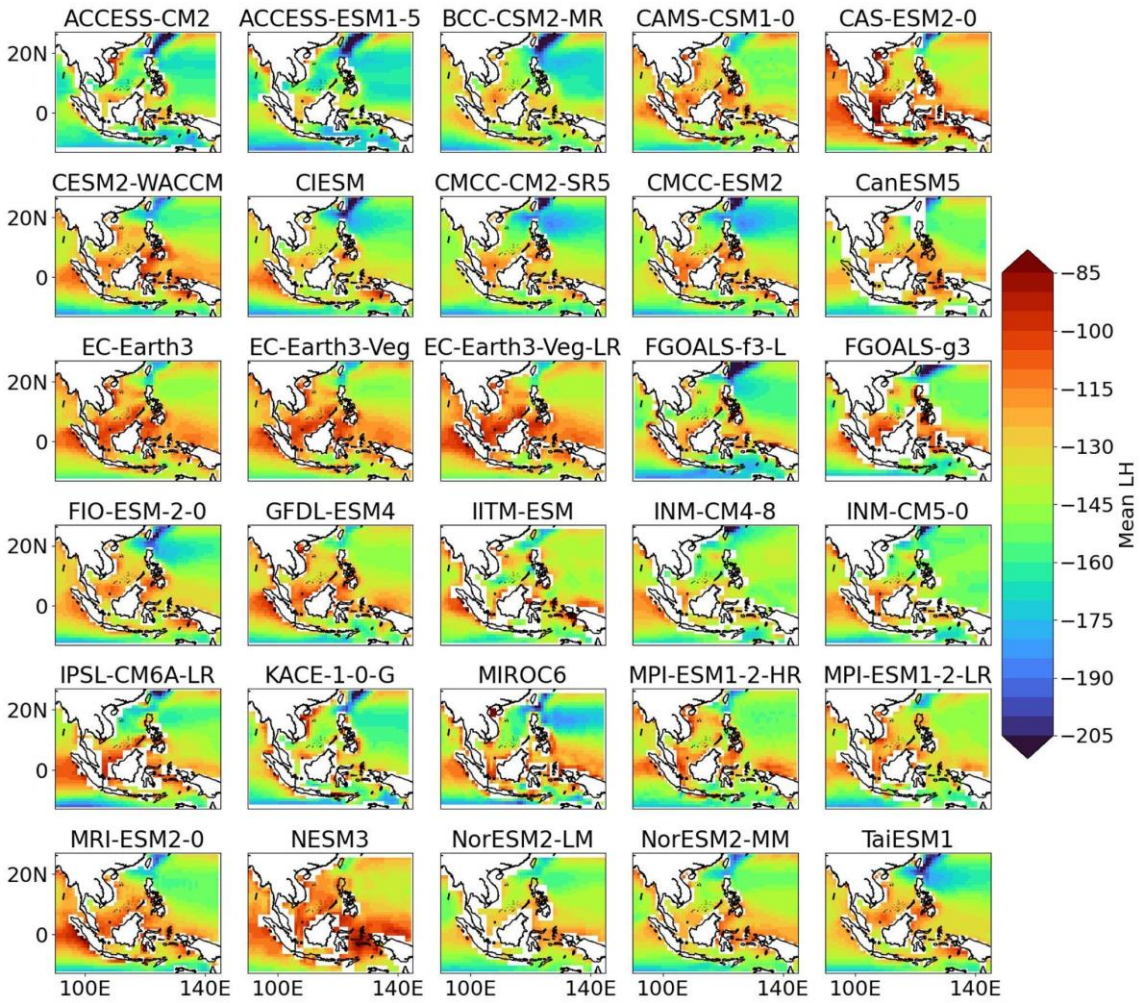

Fig. S4. As in Fig. S1, but for LH.

Accepted for publication in *Journal of Climate*. DOI 10.1175/JCLI-D-24-0389.1.

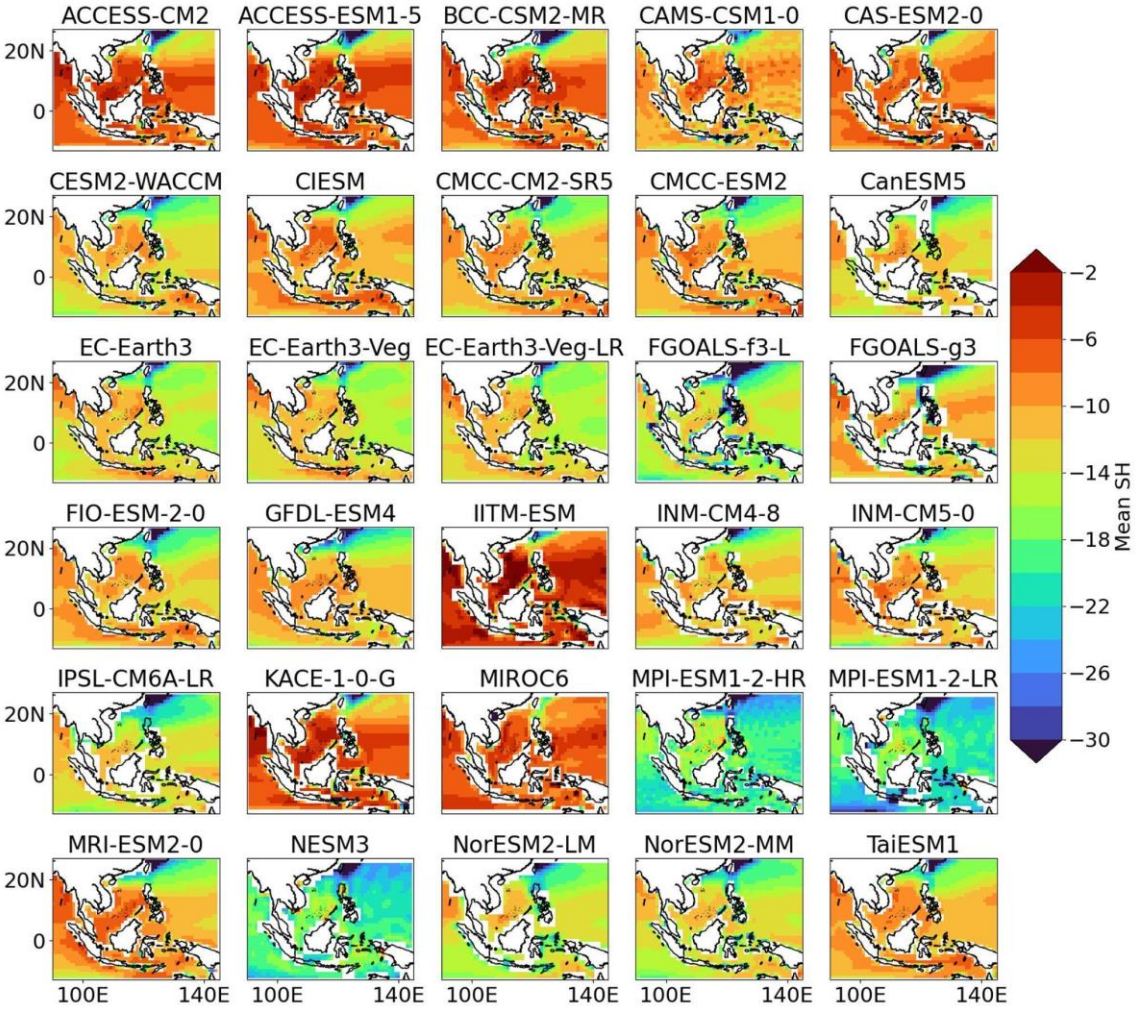

Fig. S5. As in Fig. S1, but for SH.

Accepted for publication in *Journal of Climate*. DOI 10.1175/JCLI-D-24-0389.1.

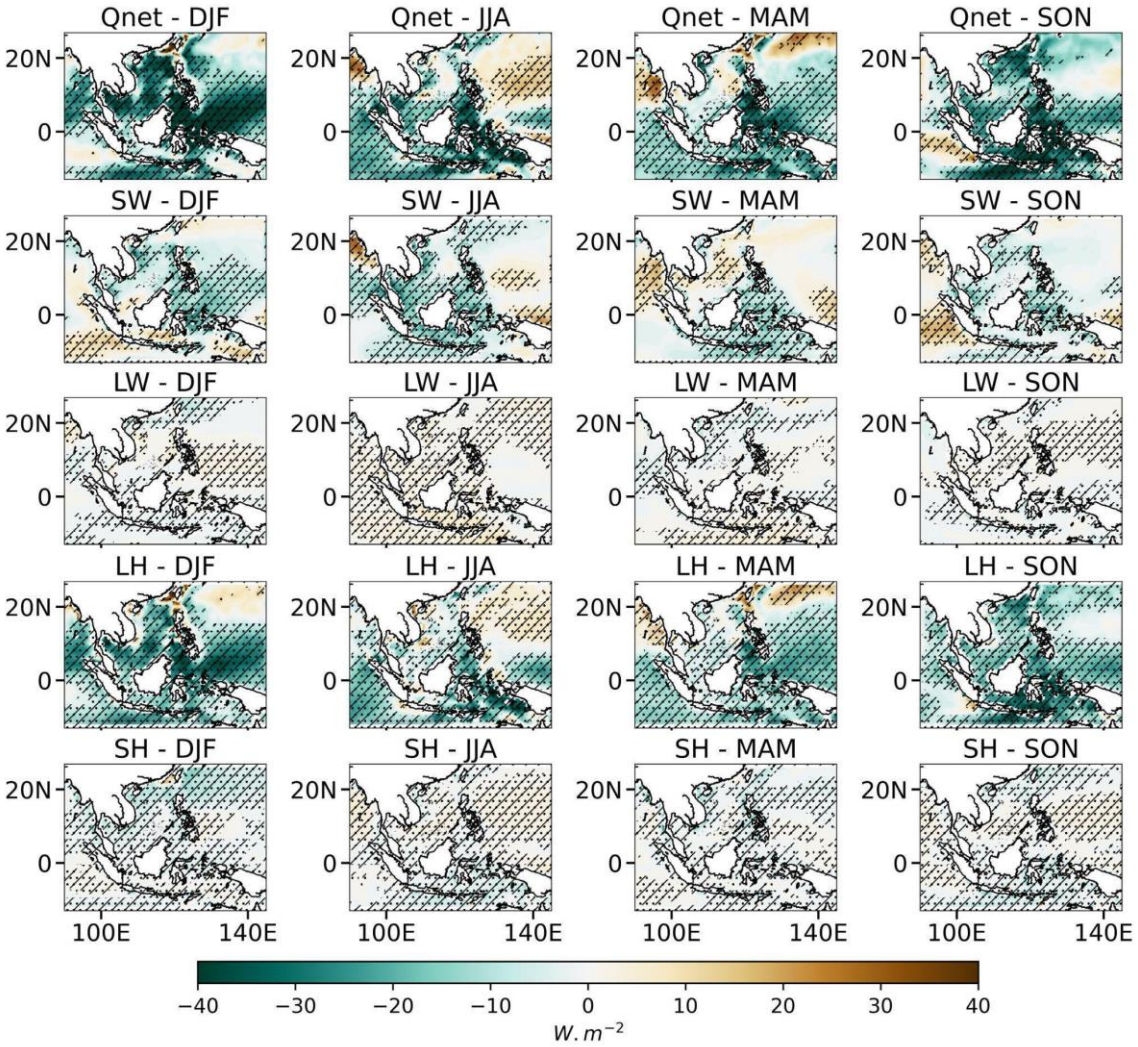

Fig. S6. Biases between CMIP6 MME and ERA5 for Qnet (1st row), SW (2nd row), LW (3rd row), LH (4th row), and SH (5th row) during DJF (1st column), MAM (2nd column), JJA (3rd column), and SON (4th column) in the baseline period (Unit: Wm^{-2}). The dot-hatch pattern indicates areas where differences are statistically significant at 95% based on the Student's t-test.

Accepted for publication in *Journal of Climate.* DOI 10.1175/JCLI-D-24-0389.1.

REFERENCES

Amaya, D.J., M.J. DeFlorio, A.J. Miller, and S.-P. Xie, 2017: WES feedback and the Atlantic Meridional Mode: Observations and CMIP5 comparisons. *Clim Dyn*, ***49***, 1665–1679, https://doi.org/10.1007/s00382-016-3411-1

Barsugli, J. J., and D. S. Battisti, 1998: The Basic Effects of Atmosphere–Ocean Thermal Coupling on Midlatitude Variability. *J Atmos Sci*, **55**, 477–493, https://doi.org/10.1175/1520-0469(1998)055<0477:TBEOAO>2.0.CO;2.

Berry, D. I., and E. C. Kent, 2009: A New Air–Sea Interaction Gridded Dataset from ICOADS With Uncertainty Estimates. *Bull Am Meteorol Soc*, **90**, 645–656, https://doi.org/10.1175/2008BAMS2639.1.

Berry, E., and G. G. Mace, 2014: Cloud properties and radiative effects of the Asian summer monsoon derived from A-Train data. *Journal of Geophysical Research: Atmospheres*, **119**, 9492–9508, https://doi.org/10.1002/2014JD021458.

Bonino, G., D. Iovino, L. Brodeau, and S. Masina, 2022: The bulk parameterizations of turbulent air–sea fluxes in NEMO4: the origin of sea surface temperature differences in a global model study. *Geosci Model Dev*, **15**, 6873–6889, https://doi.org/10.5194/gmd-15-6873-2022.

Brunke, M. A., C. W. Fairall, X. Zeng, L. Eymard, and J. A. Curry, 2003: Which Bulk Aerodynamic Algorithms are Least Problematic in Computing Ocean Surface Turbulent Fluxes? *J Clim*, **16**, 619–635, https://doi.org/10.1175/1520-0442(2003)016<0619:WBAAAL>2.0.CO;2.

Cao, N., B. Ren, and J. Zheng, 2015: Evaluation of CMIP5 climate models in simulating 1979–2005 oceanic latent heat flux over the Pacific. *Adv Atmos Sci*, **32**, 1603–1616, https://doi.org/10.1007/s00376-015-5016-8.

Cayan, D. R., 1992: Latent and Sensible Heat Flux Anomalies over the Northern Oceans: Driving the Sea Surface Temperature. *J Phys Oceanogr*, **22**, 859–881, https://doi.org/10.1175/1520-0485(1992)022<0859:LASHFA>2.0.CO;2.

Ceppi, P., F. Brient, M. D. Zelinka, and D. L. Hartmann, 2017: Cloud feedback mechanisms and their representation in global climate models. *WIREs Climate Change*, **8**, https://doi.org/10.1002/wcc.465.

Accepted for publication in *Journal of Climate*. DOI 10.1175/JCLI-D-24-0389.1.

Chang, C.-P., Y. Zhang, and T. Li, 2000: Interannual and Interdecadal Variations of the East Asian Summer Monsoon and Tropical Pacific SSTs. Part I: Roles of the Subtropical Ridge. *J Clim*, **13**, 4310–4325, https://doi.org/10.1175/1520-0442(2000)013<4310:IAIVOT>2.0.CO;2.

Chen, T., W. B. Rossow, and Y. Zhang, 2000: Radiative Effects of Cloud-Type Variations. *J Clim*, **13**, 264–286, https://doi.org/10.1175/1520-0442(2000)013<0264:REOCTV>2.0.CO;2.

Cleveland, W. S., S. J. Devlin, and E. Grosse, 1988: Regression by local fitting. *J Econom*, **37**, 87–114, https://doi.org/10.1016/0304-4076(88)90077-2.

De Deckker, P., 2016: The Indo-Pacific Warm Pool: critical to world oceanography and world climate. *Geoscience Letters*, **3(1)**, 20, https://doi.org/10.1186/s40562-016-0054-3.

Desmet, Q. and T. Ngo-Duc, 2022: A novel method for ranking CMIP6 Global Climate Models over the Southeast Asian region. *International Journal of Climatology*, **42(1)**, 97–117, https://doi.org/10.1002/joc.7234.

Dee, D. P., and Coauthors, 2011: The ERA-Interim reanalysis: configuration and performance of the data assimilation system. *Quarterly Journal of the Royal Meteorological Society*, **137**, 553–597, https://doi.org/10.1002/qj.828.

Dhage, L., & Widlansky, M. J. (2022). Assessment of 21st century changing sea surface temperature, rainfall, and sea surface height patterns in the tropical Pacific Islands using CMIP6 greenhouse warming projections. *Earth's Future*, **10**, e2021EF002524. https://doi.org/10.1029/2021EF002524

Dilley, A. C., and D. M. O'Brien, 1998: Estimating downward clear sky long-wave irradiance at the surface from screen temperature and precipitable water. *Quart J Roy Meteor Soc*, **124A**, 1391–1401, https://doi.org/10.1002/qj.49712454903

Eyring, V., S. Bony, G. A. Meehl, C. A. Senior, B. Stevens, R. J. Stouffer, and K. E. Taylor, 2016: Overview of the Coupled Model Intercomparison Project Phase 6 (CMIP6) experimental design and organization. *Geosci Model Dev*, **9**, 1937–1958, https://doi.org/10.5194/gmd-9-1937-2016.

Accepted for publication in *Journal of Climate*. DOI 10.1175/JCLI-D-24-0389.1.

Fairall, C. W., E. F. Bradley, J. E. Hare, A. A. Grachev, and J. B. Edson, 2003: Bulk Parameterization of Air–Sea Fluxes: Updates and Verification for the COARE Algorithm. *J Clim*, **16**, 571–591, https://doi.org/10.1175/1520-0442(2003)016<0571:BPOASF>2.0.CO;2.

Feng, J., T. Lian, and D. Chen, 2023: Tropical Indian Ocean Mixed Layer Bias in CMIP6 CGCMs Primarily Attributed to the AGCM Surface Wind Bias. *J Clim*, **36(12)**, 4169–4188, https://doi.org/10.1175/JCLI-D-22-0546.1.

Gao, S., L. S. Chiu, and C. Shie, 2013: Trends and variations of ocean surface latent heat flux: Results from GSSTF2c data set. *Geophys Res Lett*, **40**, 380–385, https://doi.org/10.1029/2012GL054620.

Guo, L.-Y., Q. Gao, Z.-H. Jiang, and L. Li, 2018: Bias correction and projection of surface air temperature in LMDZ multiple simulation over central and eastern China. *Advances in Climate Change Research*, **9(1)**, 81–92, https://doi.org/10.1016/j.accre.2018.02.003.

Held, I.M., B.J. Soden, 2006: Robust responses of the hydrological cycle to global warming. *Journal of Climate*, **19**, 5686–5699, https://doi.org/10.1175/JCLI3990.1.

Herrmann, M., T. Ngo-Duc, and L. Trinh-Tuan, 2020: Impact of climate change on sea surface wind in Southeast Asia, from climatological average to extreme events: results from a dynamical downscaling. *Clim Dyn*, **54**, 2101–2134, https://doi.org/10.1007/s00382-019-05103-6.

Herrmann, M., T. Nguyen-Duy, T. Ngo-Duc, and F. Tangang, 2022: Climate change impact on sea surface winds in Southeast Asia. *International Journal of Climatology*, **42**, 3571–3595, https://doi.org/10.1002/joc.7433.

Hersbach, H., and Coauthors, 2020: The ERA5 global reanalysis. *Quarterly Journal of the Royal Meteorological Society*, **146**, 1999–2049, https://doi.org/10.1002/qj.3803.

Ibrahim, H. D., and Y. Sun, 2023: Sea-surface cooling by rainfall modulates Earth's heat energy flow. *J Climate*, **36**, 5125–5141, https://doi.org/10.1175/JCLI-D-22-0735.1.

IPCC, 2021: *Climate Change 2021: The Physical Science Basis. Contribution of Working Group I to the Sixth Assessment Report of the Intergovernmental Panel on Climate*

Accepted for publication in *Journal of Climate*. DOI 10.1175/JCLI-D-24-0389.1.

Change [Masson-Delmotte, V., P. Zhai, A. Pirani, S.L. Connors, C. Péan, S. Berger, N. Caud, Y. Chen,. Cambridge University Press.

Iskandar, I., W. Mardiansyah, D.O. Lestari, and Coauthors, 2020: What did determine the warming trend in the Indonesian sea?. *Prog Earth Planet Sci*, **7**, 20, https://doi.org/10.1186/s40645-020-00334-2.

Jin, S., Z. Wei, D. Wang, and T. Xu, 2023: Simulated and projected SST of Asian marginal seas based on CMIP6 models. *Frontiers in Marine Science*, 10, https://doi.org/10.3389/fmars.2023.1178974.

Jose, D.M., and G.S. Dwarakish, 2022: Bias Correction and Trend Analysis of Temperature Data by a High-Resolution CMIP6 Model over a Tropical River Basin. *Asia-Pacific J Atmos Sci,* **58**, 97–115, https://doi.org/10.1007/s13143-021-00240-7.

Josey S.A., S. Gulev, L. Yu, 2013: Chapter 5 - Exchanges Through the Ocean Surface. *International Geophysics*, **103**, 115–140, https://doi.org/10.1016/B978-0-12-391851-2.00005-2.

Juneng, L., and F.T. Tangang, 2005: Evolution of ENSO-related rainfall anomalies in Southeast Asia region and its relationship with atmosphere–ocean variations in indo-Pacific sector. *Climate Dynamics*, **25**, 337–350, https://doi.org/10.1007/s00382- 005-0031-6.

Kalnay, E., and Coauthors, 1996: The NCEP/NCAR 40-Year Reanalysis Project. *Bull Am Meteorol Soc*, **77**, 437–471, https://doi.org/10.1175/1520-0477(1996)077<0437:TNYRP>2.0.CO;2.

Kanamitsu, M., W. Ebisuzaki, J. Woollen, S.-K. Yang, J. J. Hnilo, M. Fiorino, and G. L. Potter, 2002: NCEP–DOE AMIP-II Reanalysis (R-2). *Bull Am Meteorol Soc*, **83**, 1631–1644, https://doi.org/10.1175/BAMS-83-11-1631.

Kiehl, J. T., and K. E. Trenberth, 1997: Earth's Annual Global Mean Energy Budget. *Bull Am Meteorol Soc*, **78**, 197–208, https://doi.org/10.1175/1520-0477(1997)078<0197:EAGMEB>2.0.CO;2.

Kumar, B. P., M. F. Cronin, S. Joseph, M. Ravichandran, and N. Sureshkumar, 2017: Latent Heat Flux Sensitivity to Sea Surface Temperature: Regional Perspectives. *J Clim*, **30**, 129–143, https://doi.org/10.1175/JCLI-D-16-0285.1.

Accepted for publication in *Journal of Climate.* DOI 10.1175/JCLI-D-24-0389.1.

Large, W. G., and S. Yeager, 2004: *Diurnal to decadal global forcing for ocean and sea-ice models: The data sets and flux climatologies (No. NCAR/TN-460+STR)*.

Li, Z., T. Liu, Y. Huang, J. Peng, and Y. Ling, 2022: Evaluation of the CMIP6 precipitation simulations over global land. *Earth's Future*, **10**, e2021EF002500, https://doi.org/10.1029/2021EF002500.

Lind, R. J., and K. Katsaros, 1986: Radiation measurements and model results from R/V Oceanographer during STREX 1980. *J Geophys Res*, **91**, 13308–13314.

Magnaye, A. M. T., and Coauthors, 2023: Process-based analysis of the impacts of sea surface temperature on climate in CORDEX-SEA simulations. *Clim Dyn*, **61**, 4749–4771, https://doi.org/10.1007/s00382-023-06826-3.

Matsumoto, J., 1997: Seasonal transition of summer rainy season over Indochina and adjacent monsoon region. *Advances in Atmospheric Sciences*, **14**, 231–245, https://doi.org/10.1007/ s00376-997-0022-0.

Mayer, J., L. Haimberger, and M. Mayer, 2023: A quantitative assessment of air–sea heat flux trends from ERA5 since 1950 in the North Atlantic basin. *Earth System Dynamics*, **14**, 1085–1105, https://doi.org/10.5194/esd-14-1085-2023.

McKenna, S., Santoso, A., Sen Gupta, A., & Taschetto, A. S. (2024). Understanding biases in Indian Ocean seasonal SST in CMIP6 models. *Journal of Geophysical Research: Oceans*, **129**, e2023JC020330. https://doi.org/10.1029/2023JC020330

Meehl, G. A., 1994: Influence of the Land Surface in the Asian Summer Monsoon: External Conditions versus Internal Feedbacks. *J Clim*, **7**, 1033–1049, https://doi.org/10.1175/1520-0442(1994)007<1033:IOTLSI>2.0.CO;2.

Moseid, K. O., and Coauthors, 2020: Bias in CMIP6 models as compared to observed regional dimming and brightening. *Atmospheric Chemistry and Physics*, **20(24)**, 16023–16040, https://doi.org/10.5194/acp-20-16023-2020.

Naskar, P.R., G. P. Singh, and D.R. Pattanaik, 2024: CMIP6 projected sea surface temperature over the North Indian Ocean. *J Earth Syst Sci*, **133**, 220, https://doi.org/10.1007/s12040-024-02443-8.

Accepted for publication in *Journal of Climate.* DOI 10.1175/JCLI-D-24-0389.1.

Ngai, S. T., and Coauthors, 2022: Projected mean and extreme precipitation based on bias-corrected simulation outputs of CORDEX Southeast Asia. *Weather Clim Extrem*, **37**, 100484, https://doi.org/10.1016/j.wace.2022.100484.

Ngo-Duc, T., and Coauthors, 2017: Performance evaluation of RegCM4 in simulating extreme rainfall and temperature indices over the CORDEX-Southeast Asia region. *International Journal of Climatology*, **37**, 1634–1647, https://doi.org/10.1002/joc.4803.

Ngo-Thanh, H., T. Ngo-Duc, H. Nguyen-Hong, P. Baker, and T. Phan-Van, 2018: A distinction between summer rainy season and summer monsoon season over the Central Highlands of Vietnam. *Theor Appl Climatol*, **132**, 1237–1246, https://doi.org/10.1007/s00704-017-2178-6.

Nguyen-Duy, T., T. Ngo-Duc, and Q. Desmet, 2023: Performance evaluation and ranking of CMIP6 global climate models over Vietnam. *Journal of Water and Climate Change*, **14(6)**, 1831, https://doi.org/10.2166/wcc.2023.454.

Nguyen-Le, D., J. Matsumoto, and T. Ngo-Duc, 2015: Onset of the rainy seasons in the eastern Indochina Peninsula. *J Clim*, **28**, 5645–5666, https://doi.org/10.1175/JCLI-D-14-00373.1.

Nguyen-Le, D., T. Ngo-Duc, and J. Matsumoto, 2024: The teleconnection of the two types of ENSO and Indian Ocean Dipole on Southeast Asian autumn rainfall anomalies. *Clim Dyn*, **62**, 1–23, https://doi.org/10.1007/s00382-024-07163-9

Nguyen-Thanh, H., T. Ngo-Duc, and M. Herrmann, 2023: The distinct impacts of the two types of ENSO on rainfall variability over Southeast Asia. *Clim Dyn*, **61**, 2155–2172, https://doi.org/10.1007/s00382-023-06673-2.

Park, S., C. Deser, and M. A. Alexander, 2005: Estimation of the Surface Heat Flux Response to Sea Surface Temperature Anomalies over the Global Oceans. *J Clim*, **18**, 4582–4599, https://doi.org/10.1175/JCLI3521.1.

Pimonsree, S., S. Kamworapan, S. H. Gheewala, A. Thongbhakdi, and K. Prueksakorn, 2023: Evaluation of CMIP6 GCMs performance to simulate precipitation over Southeast Asia. *Atmospheric Research*, **282**, 106522, https://doi.org/10.1016/j.atmosres.2022.106522.

Accepted for publication in *Journal of Climate*. DOI 10.1175/JCLI-D-24-0389.1.

Pokhrel, S., U. Dutta, H. Rahaman, H. Chaudhari, A. Hazra, S. K. Saha, and C. Veeranjaneyulu, 2020: Evaluation of Different Heat Flux Products Over the Tropical Indian Ocean. *Earth and Space Science*, **7**, https://doi.org/10.1029/2019EA000988.

Qu, T., Y. Y. Kim, M. Yaremchuk, T. Tozuka, A. Ishida, and T. Yamagata, 2004: Can Luzon Strait Transport Play a Role in Conveying the Impact of ENSO to the South China Sea?*. *J Clim*, **17**, 3644–3657, https://doi.org/10.1175/1520-0442(2004)017<3644:CLSTPA>2.0.CO;2.

——, Y. Du, G. Meyers, A. Ishida, and D. Wang, 2005: Connecting the tropical Pacific with Indian Ocean through South China Sea. *Geophys Res Lett*, **32**, 1–4, https://doi.org/10.1029/2005GL024698.

——, J. B. Girton, and J. A. Whitehead, 2006: Deepwater overflow through Luzon Strait. *J Geophys Res Oceans*, **111**, https://doi.org/10.1029/2005JC003139.

Räisänen, J., 2007: How reliable are climate models?. *Tellus A*, **59**, 2–29, https://doi.org/10.1111/j.1600-0870.2006.00211.x.

Ramos, C. G. M., H. Tan, P. Ray, and J. Dudhia, 2022: Estimates of the sensible heat of rainfall in the tropics from reanalysis and observations. *International Journal of Climatology*, **42(4)**, 2246–2259, https://doi.org/10.1002/joc.7363.

Rayner, N. A., D. E. Parker, E. B. Horton, C. K. Folland, L. V. Alexander, D. P. Rowell, E. C. Kent, and A. Kaplan, 2003: Global analyses of sea surface temperature, sea ice, and night marine air temperature since the late nineteenth century. *Journal of Geophysical Research: Atmospheres*, **108**, https://doi.org/10.1029/2002JD002670.

Riahi, K., and Coauthors, 2017: The Shared Socioeconomic Pathways and their energy, land use, and greenhouse gas emissions implications: An overview. *Global Environmental Change*, **42**, 153–168, https://doi.org/10.1016/J.GLOENVCHA.2016.05.009.

Robertson, F. R., and Coauthors, 2020: Uncertainties in ocean latent heat flux variations over recent decades in satellite-based estimates and reduced observation reanalyses. *J Climate*, **33(19)**, 8415–8437, https://doi.org/10.1175/JCLI-D-19-0954.1.

Accepted for publication in *Journal of Climate.* DOI 10.1175/JCLI-D-24-0389.1.

Schneider, T., T. Bischoff, and G. Haug, 2014: Migrations and dynamics of the intertropical convergence zone. *Nature*, **513**, 45–53, https://doi.org/10.1038/nature13636

Smith, S. D., 1980: Wind Stress and Heat Flux over the Ocean in Gale Force Winds. *J Phys Oceanogr*, **10**, 709–726, https://doi.org/10.1175/1520-0485(1980)010<0709:WSAHFO>2.0.CO;2.

Song, X., and L. Yu, 2013: How much net surface heat flux should go into the Western Pacific Warm Pool? *J Geophys Res Oceans*, **118**, 3569–3585, https://doi.org/10.1002/jgrc.20246.

Sprintall, J., and Coauthors, 2019: Detecting Change in the Indonesian Seas. *Front Mar Sci*, **6**, 257, https://doi.org/10.3389/fmars.2019.00257.

Stanhill, G., and S. Cohen, 2001: Global dimming: a review of the evidence for a widespread and significant reduction in global radiation with discussion of its probable causes and possible agricultural consequences. *Agricultural and Forest Meteorology*, **107(4)**, 255-278, https://doi.org/10.1016/S0168-1923(00)00241-0.

Stephens, G. L., M. Wild, P. W. Stackhouse Jr., T. L'Ecuyer, S. Kato, and D.S. Henderson, 2012: The global character of the flux of downward longwave radiation. *J Clim*, **25**, 2329–2340, https://doi.org/10.1175/jcli-d-11-00262.1, 2012.

Supari, and Coauthors, 2020: Multi-model projections of precipitation extremes in Southeast Asia based on CORDEX-Southeast Asia simulations. *Environ Res*, **184**, https://doi.org/10.1016/j.envres.2020.109350.

Tangang, F., and Coauthors, 2020: Projected future changes in rainfall in Southeast Asia based on CORDEX–SEA multi-model simulations. *Clim Dyn*, **55**, 1247–1267, https://doi.org/10.1007/s00382-020-05322-2.

Taylor, K. E., R. J. Stouffer, and G. A. Meehl, 2012: An Overview of CMIP5 and the Experiment Design. *Bull Am Meteorol Soc*, **93**, 485–498, https://doi.org/10.1175/BAMS-D-11-00094.1.

Teutschbein, C., and J. Seibert, 2012: Bias correction of regional climate model simulations for hydrological climate-change impact studies: review and evaluation

Accepted for publication in *Journal of Climate*. DOI 10.1175/JCLI-D-24-0389.1.

of different methods. *J Hydrol*, **456**, 12–29, https://doi.org/10.1016/j.jhydrol.2012.05.052.

Thum, N., S. K. Esbensen, D. B. Chelton, and M. J. McPhaden, 2002: Air–Sea Heat Exchange along the Northern Sea Surface Temperature Front in the Eastern Tropical Pacific. *J Clim*, **15**, 3361–3378, https://doi.org/10.1175/1520-0442(2002)015<3361:ASHEAT>2.0.CO;2.

Tong, Y., and Coauthors, 2021: Bias correction of temperature and precipitation over China for RCM simulations using the QM and QDM methods. *Clim Dyn*, **57**, 1425–1443, https://doi.org/10.1007/s00382-020-05447-4.

Trenberth, K. E., J. T. Fasullo, and J. Kiehl, 2009: Earth's Global Energy Budget. *Bull Am Meteorol Soc*, **90**, 311–324, https://doi.org/10.1175/2008BAMS2634.1.

Trinh, N. B., amd Coauthors, 2024: New insights into the South China Sea throughflow and water budget seasonal cycle: evaluation and analysis of a high-resolution configuration of the ocean model SYMPHONIE version 2.4. *Geosci Model Dev*, **17**, 1831–1867, https://doi.org/10.5194/gmd-17-1831-2024.

Trinh-Tuan, L., and Coauthors, 2019: Application of Quantile Mapping Bias Correction for Mid-future Precipitation Projections over Vietnam. *SOLA*, **15**, 1–6, https://doi.org/10.2151/sola.2019-001.

U.S. Geological Survey, 1996: GTOPO30. Available online at: http://edc.usgs.gov/products/elevation/gtopo30/gtopo30.html

Valdivieso, M., and Coauthors, 2017: An assessment of air–sea heat fluxes from ocean and coupled reanalyses. *Clim Dyn*, **49**, 983–1008, https://doi.org/10.1007/s00382-015-2843-3.

Villafuerte, M.Q., J. Matsumoto, I. Akasaka, H.G. Takahashi, H. Kubota, and T.A. Cinco, 2014: Long-term trends and variability of rainfall extremes in The Philippines. *Atmospheric Research*, **137**, 1–13, https://doi.org/10.1016/j.atmosres.2013.09.021.

Wang, B. and LinHo., 2002: Rainy season of the Asian–Pacific summer monsoon. *Journal of Climate*, **15**, 386–398, https://doi.org/10.1175/1520-0442(2002)015<0386:RSOTAP>2.0.CO;2.

Accepted for publication in *Journal of Climate*. DOI 10.1175/JCLI-D-24-0389.1.

Wang, D., J. Liu, Q. Luan, W. Shao, X. Fu, H. Wang, and Y. Gu, 2023: Projection of future precipitation change using CMIP6 multimodel ensemble based on fusion of multiple machine learning algorithms: A case in Hanjiang River Basin, China. *Meteorological Applications*, **30(5)**, e2144, https://doi.org/10.1002/met.2144.

Wang, X., R. Zhang, J. Huang, L. Zeng, and F. Huang, 2017: Biases of five latent heat flux products and their impacts on mixed-layer temperature estimates in the South China Sea. *J Geophys Res Oceans*, **122**, 5088–5104, https://doi.org/10.1002/2016JC012332.

Wang, Y., T. Xu, S. Li, R. D. Susanto, T. Agustiadi, M. Trenggono, W. Tan, and Z. Wei, 2019: Seasonal variation of water transport through the Karimata Strait. *Acta Oceanologica Sinica*, **38**, 47–57, https://doi.org/10.1007/s13131-018-1224-2.

Weare, B. C., 1989: Uncertainties in estimates of surface heat fluxes derived from marine reports over the tropical and subtropical oceans. *Tellus A: Dynamic Meteorology and Oceanography*, **41**, 357, https://doi.org/10.3402/tellusa.v41i4.11846.

Wild, M., and Coauthors, 2005: From Dimming to Brightening: Decadal Changes in Solar Radiation at Earth's Surface. *Science*, **308(5723)**, 847–850, https://doi.org/10.1126/science.1103215.

Wild, M., and Coauthors, 2015: Projections of long-term changes in solar radiation based on CMIP5 climate models and their influence on energy yields of photovoltaic systems. Solar Energy, 116, 12-24, https://doi.org/10.1016/j.solener.2015.03.039.

Wild, M., 2020: The global energy balance as represented in CMIP6 climate models. *Clim Dyn*, **55**, 553–577, https://doi.org/10.1007/s00382-020-05282-7.

Wu, R., and G. Chen, 2021: Contrasting Cloud Regimes and Associated Rainfall over the South Asian and East Asian Monsoon Regions. *J Clim*, **34**, 3663–3681, https://doi.org/10.1175/JCLI-D-20-0992.1.

Wu, R., B. P. Kirtman, and K. Pegion, 2007: Surface latent heat flux and its relationship with sea surface temperature in the National Centers for Environmental Prediction Climate Forecast System simulations and retrospective forecasts. *Geophys Res Lett*, **34**, https://doi.org/10.1029/2007GL030751.

Accepted for publication in *Journal of Climate*. DOI 10.1175/JCLI-D-24-0389.1.

Wu, Z., and H. Zhang, 2024: Near-surface ocean temperature and air-sea heat flux observed by a buoy array during summer to autumn in year 2014 in the northern South China Sea. *Front Mar Sci*, **11**, 1457829, https://doi.org/10.3389/fmars.2024.1457829.

Xavier, P., R. Rahmat, W. K. Cheong, and E. Wallace, 2014: Influence of Madden-Julian Oscillation on Southeast Asia rainfall extremes: Observations and predictability. *Geophys Res Lett*, **41**, 4406–4412, https://doi.org/10.1002/2014GL060241.

Xia, F., J. Zuo, C. Sun, and A. Liu, 2023: The Atlantic Meridional Mode and Associated Wind–SST Relationship in the CMIP6 Models. *Atmosphere*, **14(2)**, 359, https://doi.org/10.3390/atmos14020359.

Yang, S., and K.-M. Lau, 1998: Influences of Sea Surface Temperature and Ground Wetness onAsian Summer Monsoon. *J Clim*, **11**, 3230–3246, https://doi.org/10.1175/1520-0442(1998)011<3230:IOSSTA>2.0.CO;2.

Yu, L., 2007: Global Variations in Oceanic Evaporation (1958–2005): The Role of the Changing Wind Speed. *J. Clim*, **20**, 5376–5390, https://doi.org/10.1175/2007JCLI1714.1.

——, 2019: Global Air-Sea Fluxes of Heat, Fresh Water, and Momentum: Energy Budget Closure and Unanswered Questions. *Annual review of marine science*, **11**, 227–248, https://doi.org/10.1146/annurev-marine-010816-060704.

——, and R. A. Weller, 2007: Objectively Analyzed Air–Sea Heat Fluxes for the Global Ice-Free Oceans (1981–2005). *Bull Am Meteorol Soc*, **88**, 527–540, https://doi.org/10.1175/BAMS-88-4-527.

——, ——, and B. Sun, 2004: Improving Latent and Sensible Heat Flux Estimates for the Atlantic Ocean (1988–99) by a Synthesis Approach. *J Clim*, **17**, 373–393, https://doi.org/10.1175/1520-0442(2004)017<0373:ILASHF>2.0.CO;2.

——, X. Jin, and R. A. Weller, 2008: Multidecade Global Flux Datasets from the Objectively Analyzed Air-sea Fluxes (OAFlux) Project: Latent and Sensible Heat Fluxes, Ocean Evaporation, and Related Surface Meteorological Variables. https://api.semanticscholar.org/CorpusID:130742744.

Accepted for publication in *Journal of Climate*. DOI 10.1175/JCLI-D-24-0389.1.

Yuan, M., T. Leirvik, and M. Wild, 2021: Global Trends in Downward Surface Solar Radiation from Spatial Interpolated Ground Observations during 1961–2019. *J Clim*, **34**, 9501–9521, https://doi.org/10.1175/JCLI-D-21-0165.1.

Zelinka, M. D., and D. L. Hartmann, 2010: Why is longwave cloud feedback positive? *Journal of Geophysical Research: Atmospheres*, **115**, https://doi.org/10.1029/2010JD013817.

Zhang, G. J., and M. J. Mcphaden, 1995: The Relationship between Sea Surface Temperature and Latent Heat Flux in the Equatorial Pacific. *J Clim*, **8**, 589–605, https://doi.org/10.1175/1520-0442(1995)008<0589:TRBSST>2.0.CO;2.

——, V. Ramanathan, and M. J. McPhaden, 1995: Convection-Evaporation Feedback in the Equatorial pacific. *J Clim*, **8**, 3040–3051, https://doi.org/10.1175/1520-0442(1995)008<3040:CEFITE>2.0.CO;2.

Zhang, R., X. Wang, and C. Wang, 2018: On the Simulations of Global Oceanic Latent Heat Flux in the CMIP5 Multimodel Ensemble. *J Clim*, **31**, 7111–7128, https://doi.org/10.1175/JCLI-D-17-0713.1.

Zhang, R., W. Guo, X. Wang, and C. Wang, 2023: Ambiguous variations in tropical latent heat flux since the years around 1998. *J Clim*, **36(10)**, 3403–3415, https://doi.org/10.1175/JCLI-D-22-0381.1.

Zhang, Y., W. B. Rossow, A. A. Lacis, V. Oinas, and M. I. Mishchenko, 2004: Calculation of radiative fluxes from the surface to top of atmosphere based on ISCCP and other global data sets: Refinements of the radiative transfer model and the input data. *Journal of Geophysical Research: Atmospheres*, **109**, https://doi.org/10.1029/2003JD004457.

Zhou, X., P. Ray, B. S. Barrett, and P.-C. Hsu, 2020: Understanding the bias in surface latent and sensible heat fluxes in contemporary AGCMs over tropical oceans. *Clim Dyn*, **55**, 2957–2978, https://doi.org/10.1007/s00382-020-05431-y.

——, 2022: Systematic improvement in simulated latent and sensible heat fluxes over tropical oceans in AMIP6 models compared to AMIP5 models with the same resolutions. *Atmos Res*, **274**, 106214, https://doi.org/10.1016/j.atmosres.2022.106214.

Accepted for publication in *Journal of Climate*. DOI 10.1175/JCLI-D-24-0389.1.

Zhou, X., P. Ray, H. Tan, J. Dudhia, R. S. Ajayamohan, H. Gomes, and Y. Pan, 2024a: Rain-induced surface sensible heat flux reduces monsoonal rainfall over India. *Geophys Res Lett*, **51**, e2023GL107796, https://doi.org/10.1029/2023GL107796.

Zhou, X., P. Ray, J. Dudhia, M. Tewari, E. Nikolopoulos, N. C. Johnson, and S. Hagos, 2024b: On the importance of precipitation-induced surface sensible heat flux for diurnal cycle of precipitation in the maritime continent. *Geophys Res Lett*, **51**, e2024GL111940. https://doi.org/10.1029/2024GL111940.

Accepted for publication in *Journal of Climate.* DOI 10.1175/JCLI-D-24-0389.1.